Timing the formation of massive bulgeless galaxies

Adrián Pérez Martín

MASTER EN ASTROFÍSICA
ESCUELA DE DOCTORADO Y ESTUDIOS DE POSGRADO
UNIVERSIDAD DE LA LAGUNA

Universidad de La Laguna

Tutores: Jairo Méndez-Abreu, Adriana de Lorenzo-Cáceres.

Dedicado a mi madre, por darme todas las herramientas necesarias para llegar hasta aquí,

a mi hermana, que por su bien espero que nunca entienda nada escrito más allá de esta página,

a mi pareja y a mi primo, por su apoyo y cariño en estos años tan complicados...

...y a mis tutores, por haber portado siempre sus estandartes en mis batallas contra el código.

Resumen

Desde sus orígenes, la humanidad se ha maravillado por su entorno, a menudo indagando en el funcionamiento del mismo. No solo el entorno cercano, sino también el cielo. La posición de las estrellas en el firmamento, el periodo de los cuerpos celestes o la sucesión de eventos como los eclipses han sido algunos de los fenómenos que han estimulado las mentes de nuestros ancestros a lo largo de nuestra historia para acercar aquello que está lejos. Este acercamiento sería especialmente notable tras la fabricación de los primeros telescopios en el siglo XVII, lo que permitiría, entre otras cosas, observar con mayor detalle la Vía Láctea y comenzar a forjar así el concepto de galaxia que conocemos hoy en día, abriendo en la década de 1920 el debate sobre la posible existencia de otras galaxias además de la nuestra. Fue Hubble quien, tras estudiar M31 (Andrómeda) en 1923, concluyó que esta no era una nebulosa contenida en la Vía Láctea, sino que se trataba de un objeto externo a la misma: otra galaxia. Tres años después, Hubble clasificaría las galaxias regulares en dos grupos principales: elípticas y espirales, cada una de ellas con sus respectivos subtipos. Mientras que las elípticas son clasificadas según su elipticidad (la relación entre los semiejes mayor y menor de su forma elíptica proyectada en el cielo), las galaxias espirales son clasificadas por la apertura de sus brazos o la presencia de una barra o bulbo central.

Los bulbos son estructuras dominadas por movimientos aleatorios, las cuales se pueden encontrar localizadas en la parte central de las galaxias de disco. Se clasifican en clásicos y de tipo disco. Los primeros se caracterizan por ser más redondos que el disco que les rodea en la galaxia, con su cinemática dominada por movimientos aleatorios que a menudo satisfacen la ecuación del plano (Bender et al. 1992; Falcón-Barroso et al. 2002; Aguerri et al. 2005) y por estar compuestos por poblaciones estelares viejas, sin formación estelar reciente. Los bulbos de tipo disco tienen una estructura más plana y su cinemática está dominada por la rotación del disco que lo rodea, clasificándose como 'outliers' de baja dispersión de velocidades (σ) de la relación de Faber-Jackson (Faber and Jackson, 1976). Los escenarios de formación y evolución de los bulbos son variados (Eggen et al. 1962; Zavala et al. 2012; Noguchi 1999; Immeli et al. 2004; Ceverino et al. 2015, entre otros). Todos ellos implican la formación de los bulbos a través de nubes masivas de gas, pero el rol de estas en dicho proceso es aún incierto. En general, no se conoce con exactitud la formación de los bulbos ni de las galaxias. El modelo más apoyado actualmente para explicar la formación de las galaxias es Λ Cold Dark Matter (ΛCDM), el cual hace uso de la Teoría General de la Relatividad y asume la existencia de materia oscura fría. Se trata de materia que no ha sido observada, pero que se necesita para explicar fenómenos presentes en el universo, como las variaciones en el fondo cósmico de microondas (CMB) o las curvas de rotación de las galaxias. Se cree que las galaxias se encuentran imbuidas en halos de materia oscura de dimensiones mucho mayores que las que ocupa su materia visible. Si bien ΛCDM consigue explicar algunos aspectos observables del universo, este predice la formación de galaxias a través de procesos de colapso de halos de materia oscura, lo cual conduce a una gran abundancia de galaxias elípticas. No obstante, las observaciones muestran una sobreabundancia de galaxias espirales respecto a esta predicción del modelo.

Aunque existen estudios previos de galaxias de tipo espiral con bulbo pequeño (Karachentsev, 1989; Kormendy et al., 2010; Méndez-Abreu et al., 2017), no se ha hecho un estudio en detalle con una gran muestra de este tipo de galaxias. Un proyecto activo que trabaja en esta dirección es Bulgeless Evolution And the Rise of Disks (BEARD), para el cual un total de 66 galaxias masivas, espirales, sin bulbo y en el universo cercano han sido seleccionadas. Este trabajo hace uso de las observaciones de dicho

proyecto que han empleado la técnica espectroscópica de rendija, las cuales suponen 33 galaxias del total en la fecha de entrega de este documento.

Para cada una de las galaxias de la muestra, se ha estudiado su espectro a distintos radios. Se ha llevado a cabo un proceso de bineado, donde se ha establecido un límite inferior en la señal-ruido (S/N) obtenida, con el fin de obtener resultados fiables en todos los radios estudiados. Por otra parte, se ha integrado el bulbo de aquellas galaxias que poseen dicha estructura, haciendo uso de la descomposición fotométrica realizada por Zarattini et al. (in prep), de la cual se ha obtenido el radio dentro del cual la luz del bulbo domina: r_{bd}. Para las galaxias sin bulbo, se ha tomado el espectro central. Tanto para los bines como para los bulbos/centros, se ha exigido una S/N mínima de 30 para ser analizados.

A cada uno de los espectros resultantes se les ha aplicado el algoritmo Penalized PiXel-Fitting (pPXF), desarrollado por Cappellari (2002), con la finalidad de obtener información sobre la cinemática y las poblaciones estelares. Dicho algoritmo ajusta el espectro dado a los modelos elegidos. En nuestro trabajo se han seleccionado los modelos desarrollados por Vazdekis et al. (2015), a partir de los datos de MILES (Sánchez-Blázquez et al., 2006). Estos modelos presentan un amplio rango de edades y metalicidades, además de dos valores distintos de $[\alpha/\mathrm{Fe}]$, parámetro que permite medir la duración de los procesos de formación estelar ocurridos en las galaxias y es inversamente proporcional a la misma. Estos modelos son novedosos en cuanto que utilizan este último parámetro como una variable, pues muchos trabajos actuales hacen usos de modelos con un único valor del mismo.

Si bien se ha obtenido información tanto para el bulbo de las galaxias de la muestra (o centro, para aquellas sin bulbo) como para distintos radios, el análisis de resultados se ha centrado en el estudio de los primeros. Esto se ha decidido así debido a las limitaciones tanto del espacio de la memoria como del tiempo de realización del TFM. Pese a ello, el estudio de los bulbos por sí mismo amerita un trabajo de esta categoría. Los resultados de la muestra han sido divididos en distintos subgrupos: galaxias con bulbo, galaxias sin bulbo, galaxias con barra (todas ellas con bulbo) y NGC1087 (pues se trata de una galaxia con un centro complejo). Esto se ha hecho con el objetivo de detectar tendencias o desviaciones de las mismas para los distintos grupos.

Se ha encontrado que las galaxias barradas parecen tener una dispersión de velocidades a lo largo de la línea de visión más baja que el resto de la muestra, pudiendo ser esto un indicador de la presencia de bulbos de tipo disco. En su mayoría, las galaxias con bulbo simple muestran una formación estelar rápida (es decir, con valores altos de $[\alpha/\mathrm{Fe}]$) de sus poblaciones más viejas, seguida por una formación más extendida en el tiempo (bajo $[\alpha/\mathrm{Fe}]$), a menudo producida hace menos de $\sim 8\,\mathrm{Gyr}$. Por lo general, las poblaciones de toda la muestra tienden a valores por encima de la metalicidad solar. Parece haberse encontrado una relación directamente proporcional entre la masa del bulbo y la duración de los procesos de formación estelar para los bulbos más masivos de la muestra (contrario a lo ocurrido para galaxias elípticas, ver Fig. 4 de Thomas and Davies 2006), si bien este resultado no es concluyente al verse limitado el rango de masa de los bulbos por emplear la muestra de BEARD. Con el fin de corroborar nuestros resultados, se han comparado estos a los de CALIFA DR3 (Sánchez et al., 2016) y a los trabajos de Morelli et al. (2008, 2016), encontrándose que son coherentes con los de este estudio. No se han visto tendencias para los subtipos de la muestra total. No obstante, es posible que el estudio en profundidad de los perfiles radiales arroje algo de luz a este respecto.

Contents

1. Introduction

Humanity has always found certain interest in all that surrounds it, including the sky. The presence of different celestial bodies like the Sun, the Moon and the stars affects the conditions down on the Earth, not only for the human race, but for the life in its entirety. Some issues like obtaining nutrients, the sleep cycle or the possibility to hunt were determined by these bodies' movement, establishing the rules under which life finds its way. However, humanity's capacity of reasoning and its mentioned interest in the sky objects made such influence to permeate deeper than for the rest of living beings. The positions of the stars at night, the period of bodies moving through the sky or the occurrence of events like eclipses were some of the aspects that stimulated our ancestors' brains to bring close that which is far away.

While some of the first theories about the celestial objects' nature were more mythical than rational, their observation helped to later develop a more elaborated and rigorous study of the sky. One remarkable figure when talking about the beginnings of the astronomy is Hipparchus ($190 - 120$ b. C.), with the elaboration of the first stellar catalogue or the first planetary model over time. This systematic study constitutes the foundation of the astronomy as a science. It is not until the XVII century that a more precise and elaborated methodology is possible thanks to the use of the first telescopes. These instruments made some features noticeable, like the presence of prominences on the Moon, spots on the Sun or the existence of satellites in Jupiter. Maybe one of the most ground-breaking findings from that era, in terms of how humanity understood the Universe, was the discovery of stars composing the Milky Way: the galaxy concept as we know it today begins to form. Later, it would be discovered that not only stars shaped the Milky Way, but also gas, dust and different bodies.

Such approach to our environment in space led to postulate the existence of other galaxies, which fostered the Great Debate (or Shapley-Curtis debate) in the 1920's. At that time, it was believed that our Galaxy was the whole Universe and the observed nebulae (some of them now known galaxies) were located inside it. Harlow Shapley (1885-1972) defended this established paradigm. On the other hand, Heber Curtis (1872-1942) stated that some of these objects were independent galaxies, this is, they were at larger distances, outside the Milky Way limits (see Shapley and Curtis, 1921, for more information about this debate). In 1923, Edwin Hubble (1889-1953) closed this crucial question when studying Cepheid stars in M31 (Andromeda), determining that their distance located the supposed 'nebula' outside the boundaries of our Galaxy (see Hubble, 1925). From that time, the concept of galaxies as stellar systems containing dust and gas (in the future, dark matter will also be considered) was established. In 1926, Hubble published a morphological classification of regular galaxies (i.e., the majority of galaxies; irregular galaxies are not considered in this study) based on his observations (see Hubble, 1926). They were first divided into ellipticals and spirals, with subtypes for each of them (see Figure 1). Ellipticals were classified by their ellipticity (the relation between the major and the minor axis of their observed elliptical shape), while spiral galaxies were classified by their positioning of the arms (open/close) or the presence of a bar or a central bulge and its size in the latter case.
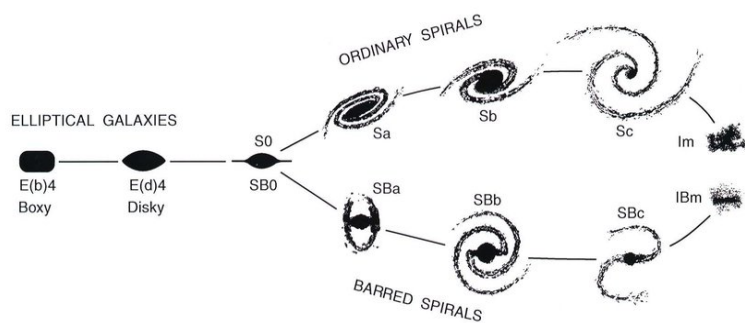

Fig. 1. Hubble morphological classification of galaxies. Figure from Kormendy and Bender (1996).

The previous Hubble classification has also generally be understood as a separation into the so called early and late type galaxies. Early-type galaxies are those with an approximately ellipsoidal shape, usually morphologically simple, without additional structures. They are dominated by random motions of the stars and typically contain old stellar populations, with no recent stellar formation. On the other hand, late-type galaxies have a disk shape, often containing spiral arms in it. They get their shape from the dominance of rotation over random motions, contrary to elliptical ones, and usually host young stars, formed in molecular gas-rich environments. However, these are not two simple groups, as there are variations between galaxies of the same general type. For example, some disk galaxies show a central structure not dominated by rotation, but by random motions: this is called a bulge. Bulges can be classified in two types: classical and disk-like. Classical bulges are characterized for being rounder than their surrounding disks. Their stellar kinematics are dominated by random motions that generally satisfy the fundamental plane correlation (Bender et al. 1992; Falcón-Barroso et al. 2002; Aguerri et al. 2005). They are usually composed of old and metal-rich (in astrophysics, elements heavier than He are called metals) stellar populations, with a short formation timescale (see Sánchez-Blázquez 2016). On the contrary, disk-like bulges have an oblate ellipsoidal shape (see Costantin et al. 2017) with an apparent flattening similar to their outer disks. Their kinematics are dominated by rotation, being identified as low-σ outliers of the Faber-Jackson relation (Faber and Jackson, 1976). Such bulges are usually composed by young stars, with the presence of gas and possible recent star formation (see Fisher and Drory 2016).

The formation and evolution scenarios for bulges are varied. They are believed to have formed from dissipative processes at high redshift, when the gas mass fraction in galaxies was higher than the current one. While some scenarios predict the bulge formed before the disk (see Eggen et al. 1962; Larson 1974; on monolithic collapse of protogalactic gas clouds or Kauffmann 1996; Hopkins et al. 2009; Zavala et al. 2012; Avila-Reese et al. 2014; on major mergers of gas-rich galaxies), some others contemplate disk formation before or concomitantly to the bulge (see Noguchi 1999; Immeli et al. 2004; Bournaud et al. 2007; Ceverino et al. 2015 on bulge formation by dynamical friction). All these models predict star formation ocurring in massive clumps, but the role of clumps in bulge formation is still unclear. Another bulge formation proposition at high redshift is related to rapid gas inflow injected to the galaxy center directly from the surrounding halo (see Scannapieco et al. 2009; Zolotov et al. 2015; Tacchella et al. 2016). At lower redshift, galaxy bulges might continue to grow through different secular processes (those involving long time-scales of the order of several galaxy rotations). Such processes could also produce the creation of new structures at the galaxies' centers, like the small bulges shown at later types of galaxies.

As for bulges, the galaxy formation and evolution process is still unclear, even after almost one hundred years from their discovery. Some of the proposed scenarios for ellipticals are similar to those for bulges that imply mergers. Among the different galaxy formation models proposed, the Λ Cold Dark Matter (ΛCDM), is the most supported nowadays. The ΛCDM model uses the General Relativity theory to explain the gravitational interaction between particles, and assumes the presence of cold dark matter in the Universe. Dark matter has been postulated and used in several models to try to explain different phenomena that require higher mass values than observed (see Zwicky, 1933, for the first evidence of this issue). Its name refers to the fact that it has not been detected, being also impossible to know its composition. It is called cold because it is assumed that it has non-relativistic velocities. This hypothetical matter is present in all of the Universe, consisting in $\sim 30\%$ of its composition and it is believed that galaxies are enclosed in a halo of dark matter, much larger than the structure where the visible material lays. ΛCDM leads to a

hierarchical galaxy formation, such as small dark matter halos are first formed, followed by their merger into bigger ones (see Figure 2). It is currently the simplest model which explains observed phenomena like the Cosmic Microwave Background (CMB), the rotation curves in galaxies or the location of galaxies in clusters distributed along filaments in the large-scale structure of the Universe. Most cosmological numerical simulations assume a ΛCDM model, and their results predict that the assembly of galaxies, due to the merging of smaller subunits, will end up either destroying the large-scale disks or creating disk galaxies with prominent central bulges (see Brooks and Christensen, 2016, and references therein). Nevertheless, observations show a relatively high fraction of bulgeless galaxies (i.e., pure-disk and galaxies with small bulges) in relation to ΛCDM predictions. It is key to know more about the observational properties of bulgeless galaxies in order to constraint better their formation and evolution. A way of doing this is studying the observational properties of their bulges, trying to unveil their most likely formation mechanism. For that purpose, it is needed not only to know the time when stellar populations were formed, but also the timescale of such event.
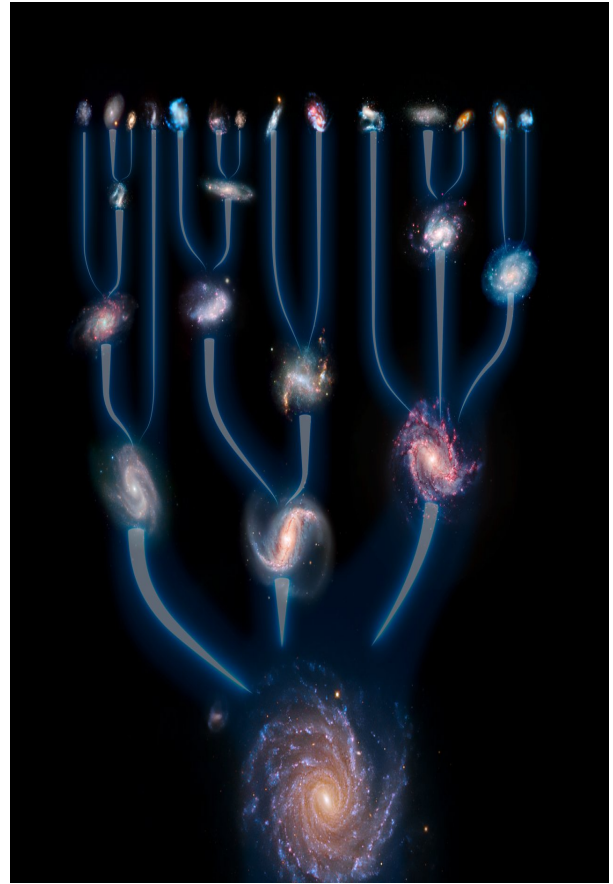
Fig. 2. Hierarchical galaxy formation according to the ΛCDM cosmological model. Credit: ESO/L. Calçada

To better understand the differences between bulges and hence theorize about their formation and evolution, it is necessary to study their content through spectra. More specifically, the spectra of their stellar populations, as galaxies are usually too far to resolve single stars. Galaxies are composed by different stellar populations, this is, stars formed at different places (with a different composition regarding the environment where they were born) and at different times. The presence of certain chemical elements, usually revealed in the form of absorption lines in the spectrum, gives information about what type of stars are populating the observed region. Studying which elements are found in a stellar population, a lower limit of the age can be estimated for such region and the galaxy itself (if attending to the oldest star population found inside it). It is common to find stellar populations with different ages in a galaxy, usually related to different structures of it (bulge, bar, disk...). By grouping those of the same age, we obtain what is called the Star Formation History (SFH), which often includes different star formation bursts. If analysing specifically the spectra of regions inside the bulge, we can obtain its SFH and therefore infer in its formation and evolution.

To study the formation timescales of stars, the relative abundance of α elements (C, O, Mg, Si, S, Ca, Ti...) with regard to the abundance of iron is used. The α elements are mainly in Type II Supernovae (SN II), that are highly energetic processes derived from the death of massive stars ($8M_\odot < M < 50M_\odot$),

which have a short lifetime. On the other hand, iron is produced in SN Ia, which are associated to binary star systems, that cover a wide range of total mass ($0.1M_\odot < M < 100M_\odot$), so they may contain low mass stars that have a longer lifetime. Then, the $[\alpha/\mathrm{Fe}]$ fraction gives a timescale in stellar formation. If by analysing the stellar populations a high $[\alpha/\mathrm{Fe}]$ fraction is obtained, this means fast stellar formation in the observed region, while a lower fraction means a slower process. This value only gives information about the length of the star formation period, but not the time when the formation occurred.

Beyond the information contained in the integrated region of the bulge structure, studying the radial profiles of stellar age and metallicity of bulgeless galaxies would help setting constraints on the formation time and physical processes leading to their observed properties. While these gradients can be obtained from theoretical models (Eggen et al., 1962; Pipino et al., 2008), there has been little progress on this topic due to the lack of a systematic study on large sample of this kind of galaxies. The first comprehensive search for disk-dominated and bulgeless galaxies was initiated by Karachentsev (Karachentsev, 1989), by observing edge-on disk galaxies, where bulges can be easily detected. After this work, the Flat Galaxy Catalog (Karachentsev et al., 1993), the Revised Flat Galaxy Catalog (Karachentsev et al., 1999) and the 2MASS-selected Flat Galaxy Catalog (Mitronova et al., 2004) were developed. Later, Kautsch (Kautsch, 2009) used Sloan Digital Sky Survey (SDSS) to study galaxies of such catalogues, finding that 16% of disk galaxies are bulgeless. However, studying only samples of edge-on disk galaxies, the presence of obscured, small and compact bulges may be hidden by dust extinction, which also prevents measuring other galaxy properties. Therefore, a systematic search for bulgeless galaxies in less inclinated galaxies is key to shed some light on their possible hierarchical formation. Previous studies of moderately-inclined bulgeless galaxies used either detailed analysis of small samples (Böker et al., 2002; Kormendy et al., 2010) or simple photometric analysis of large samples (Barazza et al., 2008; Méndez-Abreu et al., 2017), thus providing an uncertain fraction of bulgeless galaxies in the nearby Universe spanning from 20% (Barazza et al., 2008) to 74% (Kormendy et al., 2010).

One project currently working in a systematic analysis of a large sample of bulgeless galaxies is Bulgeless Evolution And the Rise of Disks (section 2), for which a total of 66 massive, bulgeless, spiral galaxies in the nearby Universe have been selected to analyse. The work presented here makes use of the long-slit spectroscopy observations from such project. More specifically, we analysed 33 galaxies of the total sample observed so far. We are focused on studying the stellar populations' properties of the bulges (or centers, for bulgeless galaxies) and their changes along the radial profiles of the whole galaxies. For that purpose, a systematic analysis for each galaxy has been carried out, expecting to expand the knowledge about the formation process of these galaxies. Since the study uses data from bulgeless, disk galaxies, which are similar to the Milky Way, it is also expected that such results aim to improve the understanding of our Galaxy. To achieve the mentioned goal, the following steps have been followed:

1. Perform a binning of the spectra of each galaxy.
2. Get the stellar kinematic parameters from the pPXF analysis of each bin.
3. Study the stellar populations by fitting each bin with pPXF, fixing the kinematic parameters to the ones obtained previously.
4. Analyse the kinematic and stellar populations results in the bulge and in a radial profile.

2. The BEARD project

The BEARD (Bulgeless Evolution And the Rise of Discs) programme is an international effort to provide irrefutable observational constraints to demonstrate the success or failure of the hierarchical ΛCDM model at forming Milky Way-like galaxies. The project studies a volume-limited sample of 66 massive ($> 10^{10} M_\star / M_\odot$), bulgeless, spiral galaxies in the nearby universe (< 40 Mpc). They have been selected from the SDSS-DR13 spectroscopic catalogue with the following conditions:

- Inclination $i < 60°$, for a good photometric definition of the bulge region and limiting the extinction from disk dust.

- Concentration $C = R90/R50 < 2.5$, to ensure the sample is dominated by late-type disk galaxies (Graham and Driver, 2005).

- Petrosian radius $R_{petro} > 10$ arcsec, avoiding extremely small galaxies where spatial resolution problems could arise.

- Total stellar mass $M > 10^{10} M_\odot$ (as obtained from the galaxy colours; Zibetti et al. 2009) in order to get a sample of massive bulgeless galaxies.

For such study, a team of 25 researchers from 6 different countries collaborate, performing observations with photometric and spectroscopic techniques. Among others, high spectral resolution spectroscopy is used to classify the central structures of the galaxies, deep broad-band photometry to characterize their outskirts looking for signs of mergers and narrow-band photometry to measure the more recent star formation.

The project aims to understand both the merger history of bulgeless galaxies and their evolution in time, in order to compare such observations with results from numerical simulations and question them. The used numerical simulations within the BEARD project are COLIBRI-EAGLE (Schaye et al., 2015) and AURIGA (Grand et al., 2017), since they overcome the spatial resolution problem when studying the radial profiles of resultant galaxies from the models.

The data from BEARD used in this work comes from the ISIS@WHT and DOLORES@TNG long-slit spectroscopy observations. Both instruments cover the necessary spectral range to study spectral features in absorption, have a spectral resolution capable of deblending the spectral lines and are setted in telescopes with diameters large enough to obtain high signal-to-noise (S/N) spectra to measure stellar populations (Morelli et al., 2016).

3. Galaxy data

For the purposes of this work, a sample of 33 galaxies, observed within the BEARD project, has been analysed. The spectra have been taken with both spectrographs ISIS and DOLORES, mounted at the William Herschel Telescope (WHT) and the Telescopio Nazionale Galileo (TNG), respectively. The two telescopes are located in Observatorio del Roque de Los Muchachos in La Palma, Canary Islands, Spain. For all the spectra analysed, the slits have been positioned parallel to the major axis of the galaxies and the spectroscopic data reduction has been previously done by other members of the BEARD collaboration. Regarding the analysis itself, both groups of images have been studied as described in the Methodology. In the following, we will describe the main characteristics of the data.

3.1. ISIS@WHT

The Intermediate-dispersion Spectrograph and Imaging System (ISIS) is a high-efficiency spectrograph ($R \sim 1000$) mounted at the f/11 Cassegrain focus of the WHT (4.2 m). It has dichroic filters, which allow to observe simultaneously in two different wavelength ranges by using two arms in the structure. The wavelength range of reduced throughput at the dichroic cross over from reflection to transmission is ~ 200 Å and it has a dispersion of $8 - 121$ Å. The default detectors installed in both arms are EEV12 (blue arm) and RED+ (red arm).

The observations obtained with this instrument have been taken using only the blue arm ($\sim 2759 - 6234$ Å), without the dichroic, since the red wavelength range contains only few lines with information on the stellar populations and without the dichroic we gain photons. The selected grism has been R300B, with a dispersion of 0.86 [Å/px] and a resolution of $R = 976$ Å, while the employed detector has been EEV12, which has 2048×4096 pixels of size 13.5 μm and a scale of 0.19 arcsec/pixel, therefore covering 216 arcsec (108 arcsec from the center). The slit positioned before ISIS for the used images has 1 arcsec $\times$ 4.0 arcmin, with an instrumental dispersion $\sigma_{\mathrm{instrum}} \sim 90$ km s^{-1} at 2.8 Å (FWHM). The list of galaxies observed with ISIS is shown in Table 1.

Galaxy	RA (J2000) [h m s]	DEC (J2000) [° ′ ″]	Bulge	DATE-OBS [y/m/d]	Slit width [arcsec]
MCG-01-09-031	03 22 17.475	-07 05 26.48	Yes	2019/12/29	1.00
NGC0514	01 24 03.897	+12 55 02.85	Yes	2019/12/29	1.00
NGC1087	02 46 25.155	-00 29 55.46	Yes	2019/12/28	1.00
NGC1090	02 46 33.936	-00 14 49.63	Yes	2020/12/28	1.00
NGC2543	08 12 57.955	+36 15 16.23	Yes	2020/02/12	1.00
NGC2701	08 59 05.755	+53 46 17.61	No	2020/02/11	1.00
NGC2742	09 07 33.575	+60 28 45.82	Yes	2020/02/12	1.00
NGC2776	09 12 14.531	+44 57 17.62	Yes	2019/12/29	1.00
NGC3294	10 36 16.256	+37 19 29.05	Yes	2019/12/30	1.00
NGC3433	10 52 03.827	+10 08 53.66	Yes	2019/12/30	1.00
NGC3756	11 36 48.026	+54 17 36.72	Yes	2020/02/12	1.00
NGC3780	11 39 22.356	+56 16 14.41	Yes	2020/02/12	1.00
NGC3888	11 47 34.332	+55 58 02.13	Yes	2020/02/13	1.00
NGC3938	11 52 49.434	+44 07 14.70	Yes	2019/12/29	1.00
NGC4062	12 04 03.809	+31 53 44.49	Yes	2019/12/29	1.00
UGC4375	08 23 11.278	+22 39 52.80	Yes	2020/02/11	1.00
UGC4621	08 50 11.810	+35 04 35.22	No	2020/02/13	1.00

Table 1: Galaxies observed with ISIS@WHT. The colums are the catalog name of the galaxy, the right angle, the declination, the presence of bulge, the date of the observation and the width of the selected slit.

3.2. DOLORES@TNG

The Device Optimized for the LOw RESolution, LRS in short, is a low resolution ($R \sim 2000$) spectrograph and camera, installed at the Nasmyth B focus of the TNG (3.5 m). It consists of a collimator, a focal reducer and a camera. The grism used in our observations is the VHR-V, with a dispersion of 0.95 [Å/px] and a resolution of R = 1527.

The default detector installed is E2V 4240, which has a total of 2048×2048 pixels with size of 13.5 μm and a scale of 0.252 arcsec/pixel, therefore covering 516 arcsec (258 arcsec from the center). The wavelength range of the spectra from DOLORES is smaller than the one from ISIS, covering $\sim 4780 - 6774$ Å. Two slits have been used for the spectra measurements of the sample, one with 0.7 arcsec $\times$ 8.1 arcmin and another one with 1 arcsec $\times$ 8.1 arcmin, with an instrumental dispersion $\sigma_{\mathrm{instrum}} \sim 60$ km s^{-1} at 2.7 Å and 3.3 Å (FWHM), respectively.

Galaxy	RA (J2000) [h m s]	DEC (J2000) [° ′ ″]	Bulge	DATE-OBS [y/m/d]	Slit width [arcsec]
IC3392	12 28 43.276	+14 59 57.96	Yes	2021/04/16	1.00
NGC3338	10 42 07.536	+13 44 49.18	Yes	2020/04/25	0.70
NGC3430	10 52 11.392	+32 57 01.55	Yes	2020/04/25	0.70
NGC3486	11 00 23.946	+28 58 29.35	Yes	2020/04/26	0.70
NGC3614	11 18 21.337	+45 44 53.52	Yes	2020/04/24	1.00
NGC3810	11 40 58.762	+11 28 15.81	Yes	2020/04/26	0.70
NGC4405	12 26 07.137	+16 10 51.58	Yes	2021/04/14	1.00
NGC5313	13 49 44.349	+39 59 05.15	Yes	2020/04/24	1.00
NGC5320	13 50 20.403	+41 21 58.38	Yes	2021/04/16	1.00
NGC5347	13 53 17.798	+33 29 27.01	Yes	2020/04/27	0.70
NGC5633	14 27 28.362	+46 08 47.52	No	2020/04/25	1.00
NGC5806	15 00 00.409	+01 53 28.78	Yes	2021/04/15	1.00
NGC5899	15 15 03.252	+42 02 59.47	Yes	2019/07/25	1.00
NGC5962	15 36 31.681	+16 36 27.93	No	2020/04/25	1.00
NGC6070	16 09 58.691	+00 42 33.27	Yes	2020/04/26	0.70
NGC6155	16 26 08.335	+48 22 00.41	Yes	2019/07/26	1.00

Table 2: Galaxies observed with DOLORES@TNG. The colums are the catalog name of the galaxy, the right angle, the declination, the presence of bulge, the date of the observation and the width of the selected slit.

4. Methodology

In this section, the analysis process for all the galaxies in the sample is detailed. For that purpose, a brief description of the Penalized Pixel-Fitting (pPXF) algorithm by Cappellari (2002) and the evolutionary stellar population synthesis from Vazdekis et al. (2015) is carried out. The steps followed to conduct such analysis have been:

1. Perform a spectral binning of the spectra for each galaxy.

2. Measure the stellar kinematic parameters from the pPXF analysis for each bin.

3. Derive the stellar population properties by fitting each bin with a pPXF version optimised to this aim.

4.1. Full spectrum fitting (pPXF) and single stellar population (SSP) models

The pPXF fitting algorithm (Cappellari, 2002) allows to fit a spectrum to a set of SSP spectra templates. For each of these templates, a weight is assigned, based on the minimization of the χ^2 value for the set of templates altogether regarding the given spectrum. The weights are higher for those templates in the set that are more similar to the stellar populations contained in the analysed spectrum. The fit has several parameters that can be tweaked according to the purposes of the analysis, like the presence of different kinematic components, the degree of the additive Legendre polynomial employed to correct the galaxy continuum shape or the masking/fit of gas emission lines in the spectra, for example. The algorithm also allows the user to select options for the output, like the elaboration of a fit plot or the calculation of high order moments of the line of sight velocity distribution (LOSVD) such as h3 and h4. From pPXF's fit, also an error estimation vector is obtained, which allows to calculate the S/N.

MILES (MIL EStrellas) is a stellar library developed for stellar population synthesis models (Sánchez-Blázquez et al., 2006). It consists of ~ 1000 stars spanning a large range in atmospheric parameters, which spectra were obtained mainly from observations with the 2.5 m INT telescope. The spectral resolution of the models from such data is 2.51 Å (FWHM) (Falcón-Barroso et al., 2011), constant with wavelenght, which is covered in the range $3525 - 7500$ Å. There is also additional data for the near IR Ca II triplet stellar library, that covers $8350 - 9020$ Å at 1.5 Å (Cenarro et al., 2001). The MILES webpage gives access to both stellar libraries and stellar populations models already developed, which can be retrieved by using their website tools[1].

The templates used to apply the pPXF algorithm to our galaxy spectra are those developed by Vazdekis et al. (2015). These models use several IMFs (for more information, see Vazdekis et al., 2003) and the scaled-solar and α-enhanced isochrones of BaSTI (Pietrinferni et al., 2004, 2006). They cover a [Fe/H] range from -2.5 to $+0.4$, with age values in the range $0.03 - 14$ Gyr for each model. Also, the values $[\alpha/\text{Fe}] = 0.0$ and 0.4 are covered, which is not usual for current empirical and semi-empirical SSP models and extends our study's possibilities. It is worth noting that such $[\alpha/\text{Fe}]$ values have been calculated using information about several α-elements' lines, while we are using it to perform a fit on Mg lines as the only α element, due to the selected wavelength range in the stellar populations analysis (subsection 4.4). In our study, not all templates from Vazdekis' models have been used. While the age range is entirely selected to cover galaxies with young and old stars (53 values), the metallicity range

---

[1]http://research.iac.es/proyecto/miles/pages/webtools/tune-ssp-models.php

is limited between -0.96 and $+0.40$ (8 values) to avoid unsafe models (see Vazdekis et al., 2015, for details). The two different values of $[\alpha/\text{Fe}]$ have been selected, as one of the goals of this analysis is to use this novelty in the fitting process of the stellar populations. Therefore, after this parameter selection, a total of 848 templates have been employed in our work. Such sample of templates are provided at $1 \, \text{M}_\odot$ and hence the results of this TFM and the plots in the shown figures are mass weighted, since the total flux of each template is not modified.

4.2. Spectral binning

Since one of the goals of this project is to study the radial profiles of both kinematic and stellar populations, we decided to carry out a spectral binning for each galaxy spectrum in order to keep the S/N of the analysed spectra over a certain threshold. Furthermore, a photometric decomposition of the sample has been performed by Zarattini et al. (in prep), so the bulge-disk radius (r_{bd}) was available for the galaxies where a bulge is present (identified in Table 1 and Table 2). This r_{bd} value is computed as the radius where the light received from the bulge equals the light received from the disk, thus measured spectra from inner radii are dominated by the bulge's light.

The spectral bins for each galaxy have been obtained in the following way. The galaxy center has been selected from the maximum value of the spectrum integrated along the wavelength axis. The pPXF fit is then carried out for the spectrum at such center (i.e., covering the pixels associated with the different wavelengths) and a S/N value is obtained. The signal (S) is taken as the median signal in the $5100 - 5500$ Å wavelength range, while the noise (N) is estimated as the standard deviation of the difference between the galaxy spectrum and the resultant fit in that same wavelength range. If the obtained S/N is not above a certain threshold, the spectrum of one row at a larger radius is added (summed) to the previously used spectrum. This process is done recursively until the minimal S/N is reached or until there are no more rows of the image in such direction, so the distance from the center is only limited by the measured S/N. This binning is first performed from the center (included) to the superior image border. Then, it is done for the rest of the illuminated pixels below, starting from the row right under the center. In this notation, the center is established as 0, with the rows above presenting a plus sign and the ones below, a minus symbol. A new FITS image is then created with the spectra of the different bins, and a CSV file is saved with information about the pixels selected for each bin.

The binning has been carried out for both S/N=20 and 30 thresholds for 5 galaxies (NGC2701, NGC3294, NGC4405, NGC5806 and NGC5962). This allowed to test the quality of the kinematic fit for two different S/N before systematically binning all the sample (see Figure 3). While the lower threshold allows to reach more distant radii, the resultant fits were less reliable with distance from center due to decrease in the depth of the absorption lines of the spectra. Since the stellar populations analysis requires a fit of the spectra which is highly sensible to the absorption lines, the S/N=30 threshold has been used for the binning process. This way, the reached distance from the center decreases, but the fitting to those spectra is more reliable. Therefore, all results shown in this TFM have been obtained using a S/N=30 threshold for the resulting spectra from the binning. In Table 3 we show the maximum extension of the binned data for each galaxy.

a) Binning for S/N=20 threshold

b) Binning for S/N=30 threshold
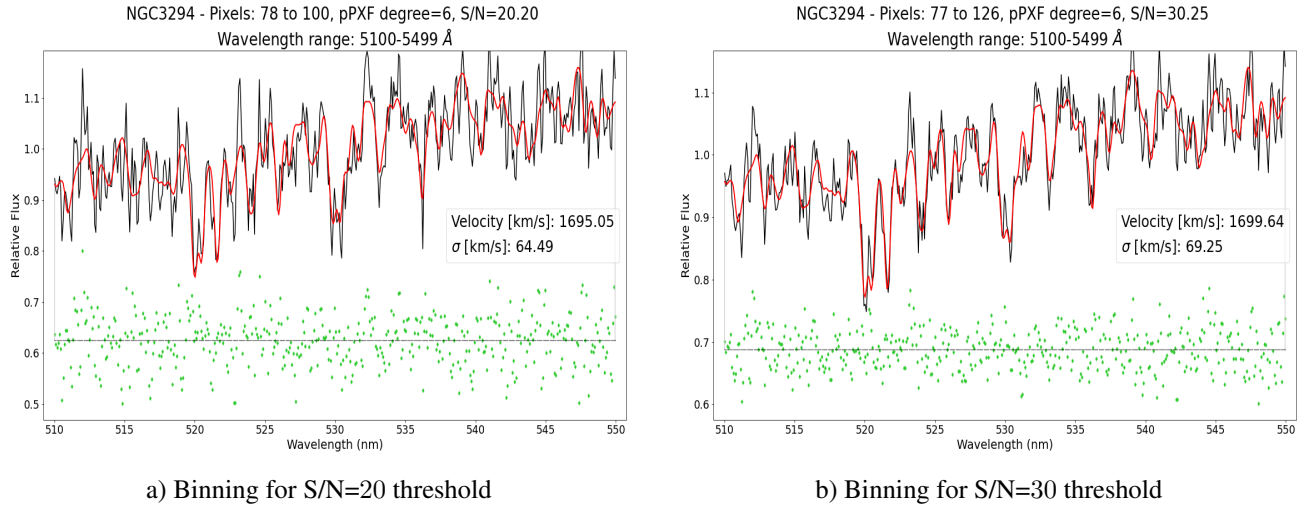
Fig. 3. Fitting comparison between both threshold values (S/N=20 and 30) for the binning process for NGC3294. The black line is the spectrum of the galaxy at its center, the red line is the best fit obtained by pPXF and the green dots are the residuals, with their median represented as a black horizontal line. The lines are better fitted for the higher threshold and the noise is lower and more constant.

For the study of the bulge, the center has been selected as for the binning process. From such central position, the spectra within the r_{bd} in both slit directions is summed into a single spectrum and considered the characteristic spectrum from the bulge of the galaxy. It is important to note that r_{bd} is not a definition of the boundaries of the bulge itself, so there may be contamination from the disk light in the analysed spectra of the galaxies' bulges. For the galaxies without a bulge, the spectrum at the estimated center has been selected for comparison.

4.3. Stellar kinematic

For the kinematic analysis of the spectra, the fits using pPXF have been done for the median-normalized spectra of the galaxies, with a constant, arbitrary noise input vector. The templates have also been normalized by the median of all of them together. Despite such normalization not being mandatory for the kinematic fit (neither for the galaxies' spectra or the templates), it has been carried out to be consistent with the process done for the stellar populations analysis. We used an additive Legendre polynomial of degree 6 to correct for possible problems in the stellar continua due to poor spectrophotometric calibration or flat-field correction issues. A single kinematic component has been assumed for all the galaxies in the sample, for which the first two moments of the LOSVD have been retrieved: velocity and velocity dispersion. The selected wavelength range for the kinematic fitting was $5100 - 5500$ Å, since it does not contain sky lines and is close enough to the range used for the stellar populations analysis, so the estimated S/N value is representative for it too. An example of the kinematic fit to one spectra is shown in Figure 4.
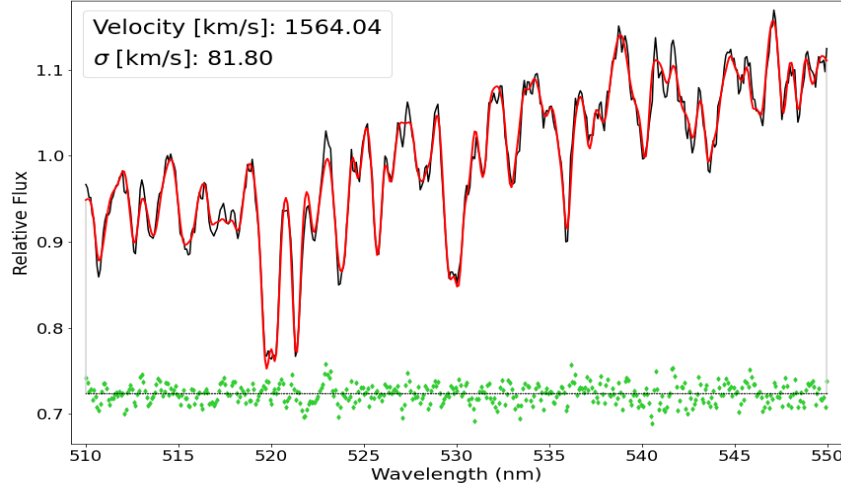
Fig. 4. Example of kinematic fit for NGC3294's bulge integrated spectrum. The black line is the galaxy bulge spectrum, the red line is the best fit obtained by pPXF and the green dots are the residuals, with their median represented as a black horizontal line. The first two moments of the LOSVD obtained from the fit are shown in a chart.

The kinematic analysis has been applied to the binned images of the different galaxies and the integrated bulge spectra (both described in subsection 4.2). This gave a radial profile of the kinematic quantities for the entire sample. For both the bins and the integrated spectrum of the bulge (or the center, if the galaxy has no bulge), the obtained information has been: the mean signal, the estimated noise from the fit, the S/N from the previous values, the velocity, the velocity error, the velocity dispersion and the error of the velocity dispersion. For the bins, also the pixels covered in the image have been included in the final table, while for the bulge it has been done for the center and the r_{bd}.
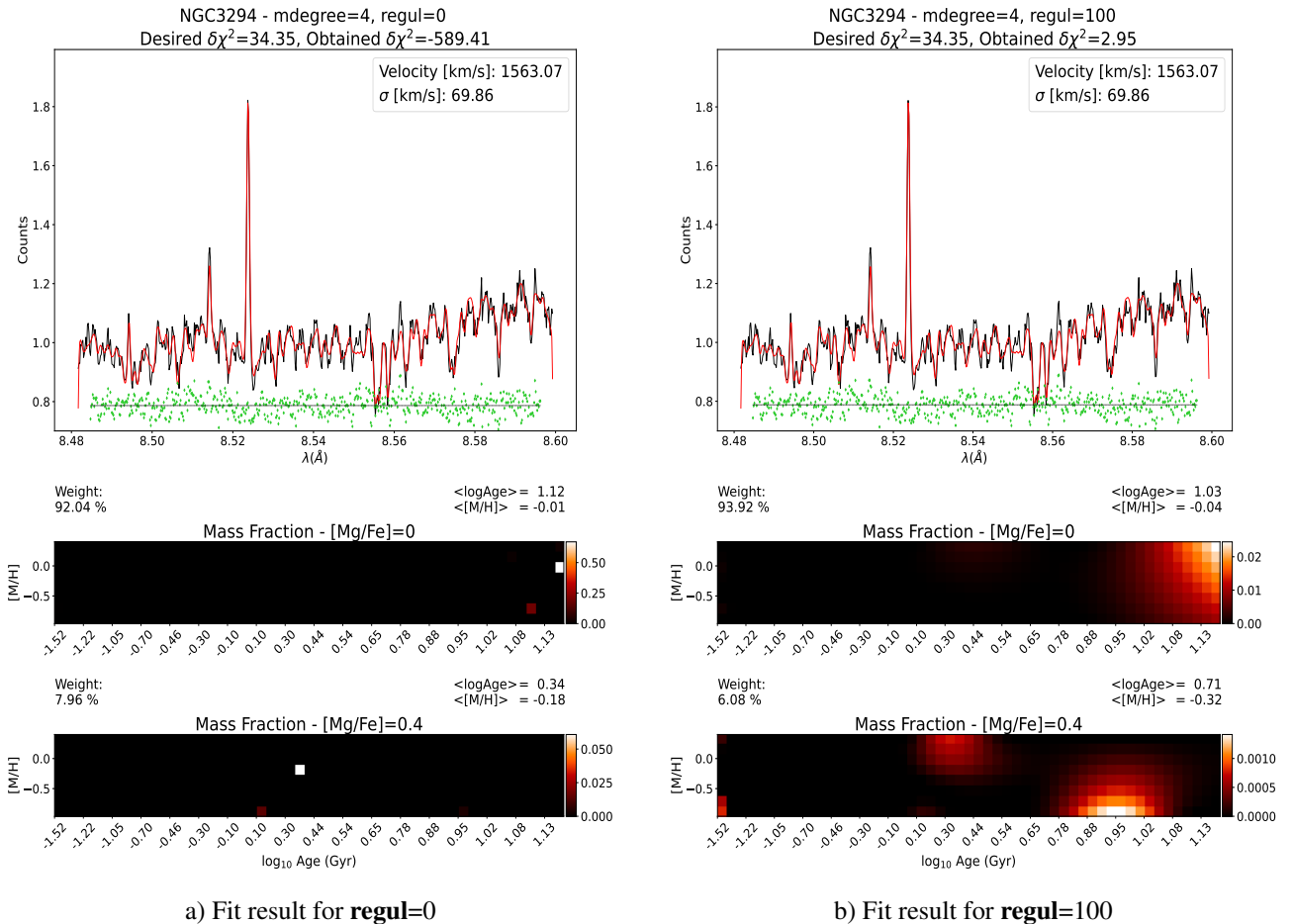
4.4. Stellar populations

The pPXF algorithm in its stellar population optimised version is used to fit the spectra, this time fixing the kinematic parameters to the results previously obtained. This is done to reduce the velocity dispersion/element abundance degeneracy on the broadening of the absorption lines (Sánchez-Blázquez et al., 2011). The selected wavelength range is $4800 - 5400$ Å, where the Hβ line, which is sensitive to age, and different lines of Magnesium and Iron are located, resulting in a versatile range to study age, metallicity and $[\alpha/\text{Fe}]$ without fitting several components. Furthermore, this range was previously used by Scholz-Díaz et al. (2022), proving it is the best range to select for our goals. A multiplicative Legendre polynomial of degree 8 has been selected. The noise has been obtained from the previously carried out kinematic fit, considering it a constant array of $1 - std$, being std the standard deviation of the difference between the galaxy and the best fit spectra. From this fit, the mean age and metallicity for both $[\alpha/\text{Fe}] = 0$ and 0.4 have been obtained, along with the total mass weight from pPXF for each of the $[\alpha/\text{Fe}]$ values.

One of the key parameters used for this stellar population analysis is the regularization factor (the **regul** parameter for pPXF's function). It smoothens the weights obtained for the templates, which is useful to try to attach a physical meaning to them, in terms of star formation and chemical composition.

For that, the templates have been sorted by age and metallicity. The larger the regularization factor value, the stronger the softening. To get some perspective of the regularization effect, both the non-regularized weights result and the regularized one have been compared in Figure 5. The two top panels show the result of the stellar population analysis without (left) and with (right) regularization. For both of them, the fitted spectrum is plotted (black) along with the best fit obtained by pPXF (red). To get a better estimation of the fit accuracy, the noise vector (green) calculated as the difference between the galaxy spectrum and the best fit is plotted, using a black horizontal line to mark the median noise value. Below the fit representation panel, there are the weights of each one of the individual templates used in the fit, separated by $[\alpha/\text{Fe}] = 0.0$ (middle panels) and 0.4 (bottom panels). The assigned weights are proportional to the likelihood of the analysed spectra of belonging to a stellar population with the template's values of age, metallicity and $[\alpha/\text{Fe}]$. It is worth noting that the color maps of such weights have different scales despite using the same color scheme, as that is only for visual clarity.

a) Fit result for **regul**=0   b) Fit result for **regul**=100

Fig. 5. Stellar populations results for the integrated bulge spectrum of NGC3294 for two regularization factors (**regul** $= 0$ and 100). The top panel in each figure shows the analysed spectrum (black) along with the best fit found by pPXF (red) for the used templates and the residuals (green) with their median (black horizontal line). The middle and bottom panels show the weights of all the used templates for $[\alpha/\text{Fe}] = 0.0$ and 0.4 templates, respectively. The effect of the regularization factor is seen in the distribution of the weights, which is smoother for **regul**=100.

From Figure 5 it is visible that not using the regularization factor may lead to separate stellar populations having a substantial difference in their ages and [M/H]. While it is possible and not unusual to find different bursts of stellar formation, it is not expected that all their stars concentrate in a single value of age and metallicity. These resulting weight composition, with 'isolated' pixels of high value are a result of the mathematical procedure employed by pPXF and do not represent exactly the stellar population distribution of age and metallicity values. Since star formation takes some time (which determines the value of $[\alpha/\mathrm{Fe}]$) and stars are formed from gas, which is not perfectly homogeneous in composition, a more diluted distribution of the weights is anticipated. This is seen for **regul**=100, where there is a more homogeneous distribution of the weights, coherent with the positions of the ones obtained without regularization. Although regularization is desirable to attach a physical meaning to the weights, its value has to be carefully selected to avoid results that may be mathematically smooth, but do not represent the real distribution of age and metallicity values in the analysed spectra. To study this effect, different regularization factors have been tested. The pPXF manual provides a procedure to obtain the **regul** value for a spectrum that minimizes the χ^2 and its derivative. The process is the following:

1. Perform an un-regularized fit (**regul=0**) and then rescale the input noise spectrum so that χ^2/DOF $= \chi^2/\mathrm{goodPixels.size} = 1$.

2. Increase **regul** and iteratively redo the pPXF fit until the χ^2 increases from the unregularized value $\chi^2 = \mathrm{goodPixels.size}$ by $\Delta\chi^2 = \mathrm{sqrt}(2*\mathrm{goodPixels.size})$.

where DOF stands for degrees of liberty and is given by $\mathrm{goodPixels.size}$, the number of pixels used in the fitting, that may be selected manually with a mask or detected by the pPXF itself if not given.

While following these steps we have obtained the desired χ^2 and $\mathrm{DeltaChi}^2$, it led to extremely large values of the regularization factor (several orders above **regul** ~ 100) for $\sim 90\%$ of the sample. Large values give results which highly divert from the unregularized ones, misrepresenting the distribution of values in the stellar population analysed. Such deviations usually shift to old, metal-rich templates, as they favour the smoothening of the weights due to the small differences between stellar populations of old ages (see Figure 6). Furthermore, the regularization value seemed to increase with distance from center, probably due to the binning process mixing several stellar populations, as the bin size increases with radii due to the decrease of the S/N in the slit image. After several tries, the regularization parameter has been set to 100, as advised by the pPXF documentation. Hence, the resulting process for the stellar populations analysis has been simplified:

1. Perform an un-regularized fit (**regul**= 0) and then rescale the input noise spectrum so that χ^2/DOF $= \chi^2/\mathrm{goodPixels.size} = 1$.

2. Perform a fit with **regul**= 100 and retrieve the results.

After carrying out the stellar populations analysis with the procedure described above, we obtain a plot like the ones shown in Figure 5, with the performed fit and their associated templates' weights for each bin of the galaxy. By applying the weights to the age and metallicity values of the corresponding templates, both average values for the two $[\alpha/\mathrm{Fe}]$ are obtained and saved along with the kinematic previous values. The total weight values for both $[\alpha/\mathrm{Fe}]$ are also saved to allow the calculation of the mean values for all the sample.
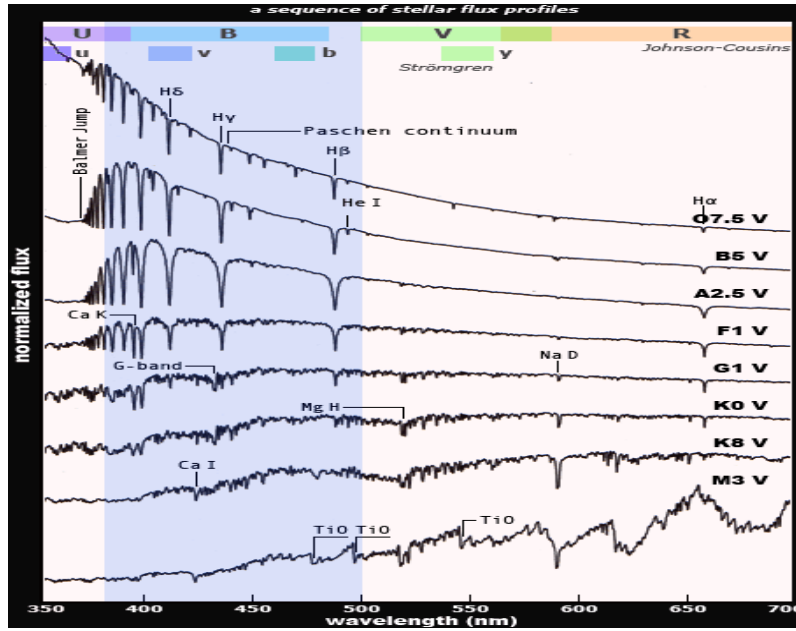
Fig. 6. Spectra of different star types. It can be seen how the stellar populations composed of youngest stars (O, B, A... types) are more distinguishable from others than the oldest ones (K types). Image obtained from https://www.handprint.com/ASTRO/specclass.html.

5. Results and discussion
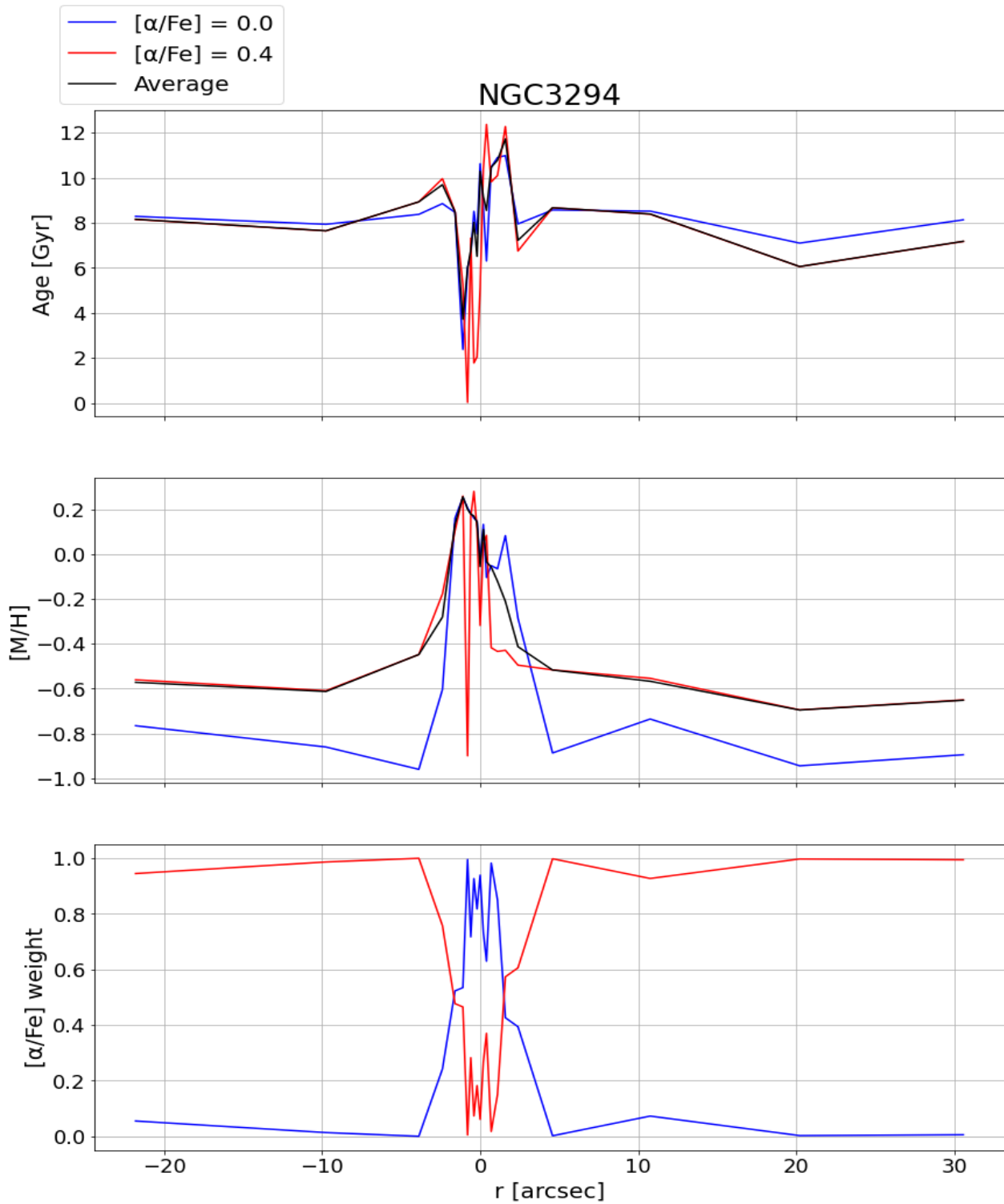
5.1. Radial profiles

One of the goals of our work was to perform radial profiles for the different physical quantities of the galaxies contained in the analysed sample. The binning code has been applied to all of them and their maximum reached radii are shown in Table 3. Then, the results from the stellar kinematic analysis have been represented like for the shown example in Figure 7. The rotational velocity of the galaxy relative to the center is seen in the decrease/increase of the total velocity to the left and to the right, respectively. However, it may be possible that the center is slightly displaced to the left in view of the horizontal line at that position. Since this profile has been calculated for each of the bins independently, it points that the fitting process seems to have worked correctly, as it reproduces the rotation curve. In the second panel, we see that the velocity dispersion has a minimum at the center (~ 70 km/s) to then increase when augmenting radii (at ~ 92.5 km/s to the left and ~ 102.5 km/s to the right). After that, the peaks at both radial directions decrease to ~ 75 and 67.5 km/s, respectively. Then, the behaviour splits in each direction: to the left it increases up to ~ 95 km/s to then slowly decrease, while to the right the velocity dispersion seems relatively constant at ~ 70 km/s to then start slowly rising. The changes in the velocity dispersion are usually related to the presence of different structures (classical bulges show more elevated velocity dispersions than disk-like ones or disks, for example). For the example here studied, NGC3294, a symmetrical behaviour is shown close to the center, which could be related to its bulge being classified as a classical one. However, specially when reaching larger radii, some radial asymmetries seem to arise in the disk.

17
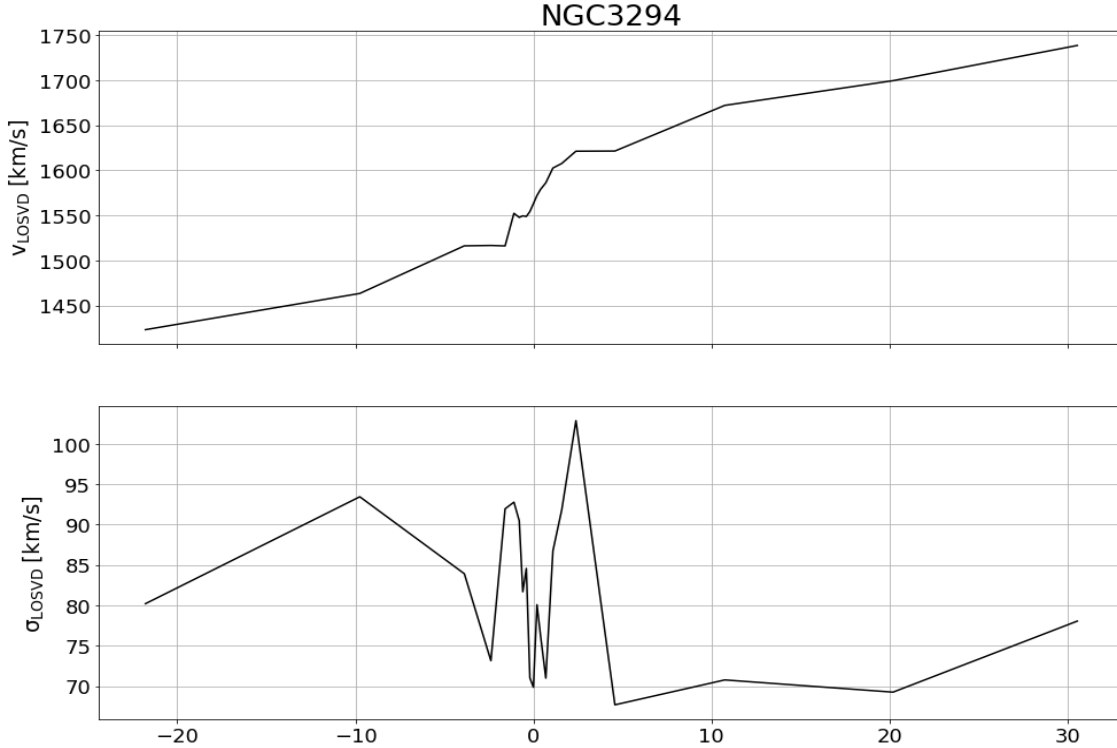
Fig. 7. Radial profiles of velocity (top panel) and velocity dispersion (bottom panel) for NGC3294. Both quantities refer to the LOSVD and the plotted velocity contains the recession velocity of the galaxy.

The age and metallicity profiles have also been plotted for each galaxy, along with the radial distribution of the $[\alpha/\text{Fe}] = 0$ and 0.4 weights like shown in Figure 8. From the top panel, it can be seen how the hinted displacement of the center from the velocity curve in Figure 7 is supported by the asymmetry of the age profile from the estimated center. The same is observed in the intermediate panel, where metallicity is represented. However, this possible error in the center selection is not visible in the $[\alpha/\text{Fe}]$ plot, at the bottom panel. If we consider that the center locates at the minimum value of the age in the top panel, then when increasing radii, we see how age increases too, to then slightly fall and remain mostly constant in both directions. This profound decrease of age in the center could be due to new (~ 4 Gyr vs the ~ 12 Gyr age of the galaxy) star formation produced by the inflow of metal-rich (intermediate panel) gas to the galaxy center. Such formation supposed a slow-paced process relatively to previous star bursts in NGC3294, as deduced from the bottom panel, where the $[\alpha/\text{Fe}]$ profile is shown. The age and metallicity trends are coherent with the rise and fall of the velocity dispersion with radii seen in the bottom panel of Figure 7.

Since the study of the radial profiles requires the exhaustive analysis of each one of them, it has been prioritized to analyse the results of the entire sample, searching for trends of galaxies with similarities. This has to be done with regions that are equivalent, which requires a photometric decomposition to delimit the structures of each galaxy to compare. Such study of the sample behaviour as a whole has been done for the bulges (and centers, for the bulgeless galaxies) and its detailed in subsection 5.2. As for the radial profiles, their in-depth analysis is left as remaining work for Pérez-Martín et al. (in prep), an extension of this TFM.

Fig. 8. Mass-weighted radial profiles of age (top panel), $[\mathrm{M/H}]$ (intermediate panel) and $[\alpha/\mathrm{Fe}]$ weights (bottom panel) for NGC3294. The blue lines refer to the results from $[\alpha/\mathrm{Fe}] = 0$ templates, while the red ones do to the $[\alpha/\mathrm{Fe}] = 0.4$. The average between these two is represented by the black line for age and $[\mathrm{M/H}]$.

5.2. Integrated properties of bulges

For the bulges, the stellar kinematics and stellar populations results will be described in this section. We have highlighted galaxies in the sample according to their central structures: with bulge (dot), without bulge (triangle) and with bar (cross). It is worth to remark that for the galaxies without a bulge, the spectrum at the center of the galaxy is analysed. Also, all barred galaxies of our sample have a bulge. The galaxy NGC1087 has been also differenced (star), as it has a complex structure at the center, so this could help detecting deviations of it from the rest of the sample. Galaxies NGC2742, NGC2701 and UGC4621 have resulted in a bulge spectrum of S/N lower than 30, so they have been excluded from this analysis. Figure 9 shows the kinematic results obtained for the bulges and centers of the sample galaxies.
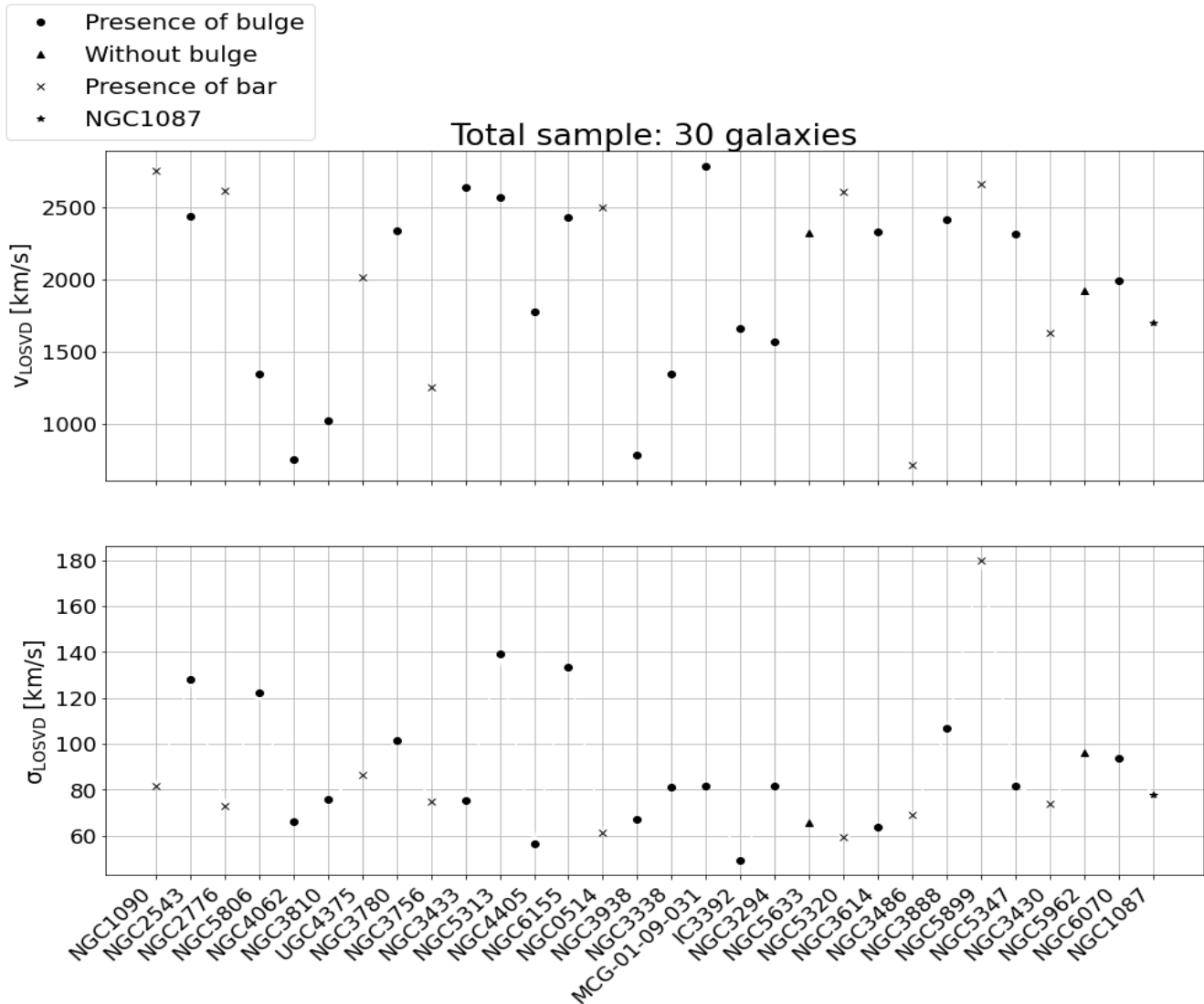
Fig. 9. Kinematic parameters obtained for the galaxies' bulges and centers (for the pure bulgeless cases). The top panel shows the obtained line of sight velocities for the different bulges, without subtracting the recession velocity of the galaxy. The bottom panel shows the line of sight velocity dispersion results for all the sample. Galaxies with bulge (black dot), without bulge (black triangle), with bar (black cross) and NGC1087 (black star) are distinguished.

In general, the velocity dispersion values for our sample are low ($< \sigma > \sim 85 \pm 31$ km/s). This is consistent with our sample being selected to host small bulges or being completely bulgeless. In the figure above, it can be seen that galaxies with bulges have different dispersion values. This is not the case for the barred galaxies, for which the velocity dispersion does not go above $\sigma \sim 90$ km/s. It is similar for the bulgeless galaxies, where the velocity dispersion stays below $\sigma \sim 100$ km/s. The slight difference between barred and non-barred galaxies of the sample might hint towards bulges in barred galaxies usually being more disk-like, i.e., built by secular processes due to the bar. One exception is the barred galaxy NGC5899, for which the obtained dispersion is $\sigma \sim 180$ km/s. The stellar kinematic and population fits have been revised to search for possible errors for this galaxy. However, a S/N = 123 has been obtained for its bulge spectrum and the fit has been correctly performed (see Figure 10). Therefore, in order to understand this result, we have searched for relations of the velocity dispersion with the properties of the sample galaxies.
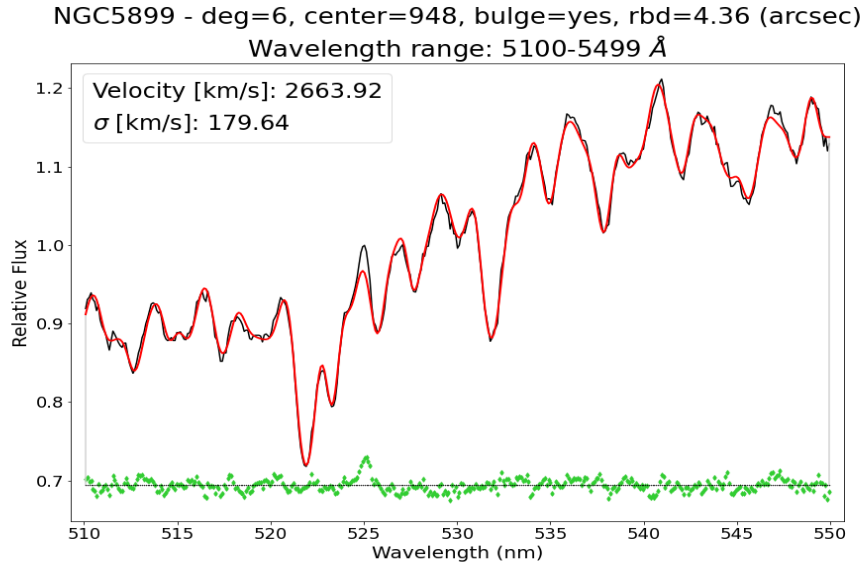
Fig. 10. pPXF fit for the integrated bulge spectrum of NGC5899. The bulge spectrum is plotted in black, the obtained fit in red and the residuals from such fit in green, with their median as a black horizontal line.

From Figure 11, there seems to be a correlation between the bulge mass and its LOSVD velocity dispersion. Such masses have been calculated from the photometric decomposition (Zarattini et al., in prep) used to select the bulge region to integrate (below the r_{bd} value). It is worth remembering that the BEARD sample contains massive galaxies with low mass bulges, which restricts the range of bulge masses. NGC5899 presents the most massive bulge from all the sample, with the highest σ value. The less massives bulges at ~ 7.5 M$_\odot$ (NGC1087 among them) do not seem to follow this apparent trend and even one of these bulges is a clear outlier with a high velocity dispersion of ~ 130 km/s (NGC6155). Furthermore, no different trends are found for bulge and bulgeless galaxies or for barred ones, except for the examples mentioned above.
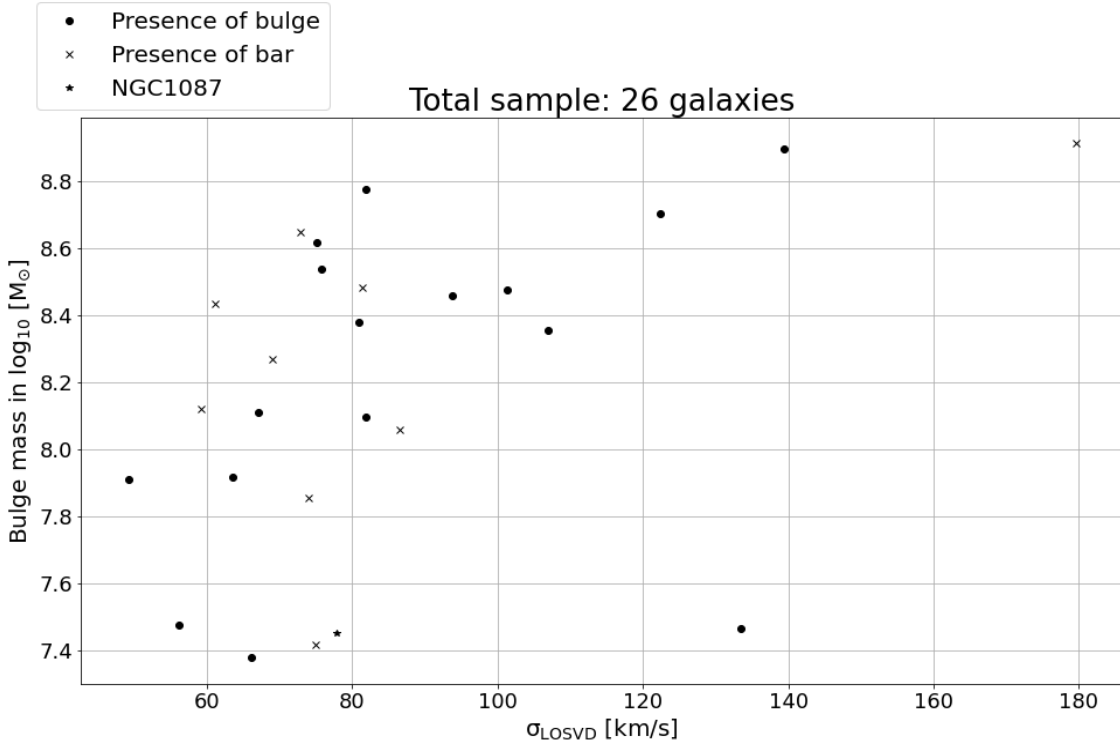
Fig. 11. Relation between the bulge mass and the velocity dispersion (LOSVD) obtained from pPXF fitting. Galaxies with bulge (black dot), with bar (black cross) and NGC1087 (black star) are distinguished.

The measured mean mass-weighted age and metallicity values from the stellar populations analysis are represented in Figure 12, along with the weights for both $[\alpha/\text{Fe}] = 0$ and 0.4 templates. It is clear that, for most of the galaxies of the sample, the dominating value is $[\alpha/\text{Fe}] = 0$, implying a slow star formation process. Separating the results for the 2 possible values of $[\alpha/\text{Fe}]$, we found that for $[\alpha/\text{Fe}] = 0$, the ages cover all the templates range, but most of the galaxies with bulge and without a bar (a 88% of the 18) have had such formation less than ~ 8 Gyr ago. Although a large timescale formation usually dominates the bulges (using $[\alpha/\text{Fe}] = 0$ as a proxy), barely all of them (except for NGC1087) have contributions larger than 10% from the $[\alpha/\text{Fe}] = 0.4$ populations. Aside from NGC3433, NGC6155 and NGC3614, all galaxies with bulges show older ages for the fast-forming ($[\alpha/\text{Fe}] = 0.4$) stellar populations than for the slow forming ($[\alpha/\text{Fe}] = 0$) ones. This scenario can be understood as an old population formed in a short burst long ago, followed by a younger formation process more extended in time. One of the bulge-less galaxies (NGC5633) and four of the barred (UGC4375, NGC3756, NGC5320 and NGC5899) also oppose this scenario, implying 50% and 44% of their respective subsamples. NGC1087 does not follow this SFH either, even being its $[\alpha/\text{Fe}] = 0.4$ equivalent to 0. Regarding the metallicity results, most of the slow-forming populations (a 76% of them) locate above the solar metallicity. Despite this being also the behaviour for the fast-forming populations (with a 66% of them above $[\text{M/H}] = 0$), the latter usually tend to lower values than the slow-forming ones: the mean metallicity values are $[\text{M/H}] = 0.1$ and -0.02 for the $[\alpha/\text{Fe}] = 0$ and 0.4 populations, respectively. To better visualize the obtained results according to the age and metallicity range from the templates, histograms for both quantities have been performed for all the sample and for the barred galaxies alone (Figure 13).
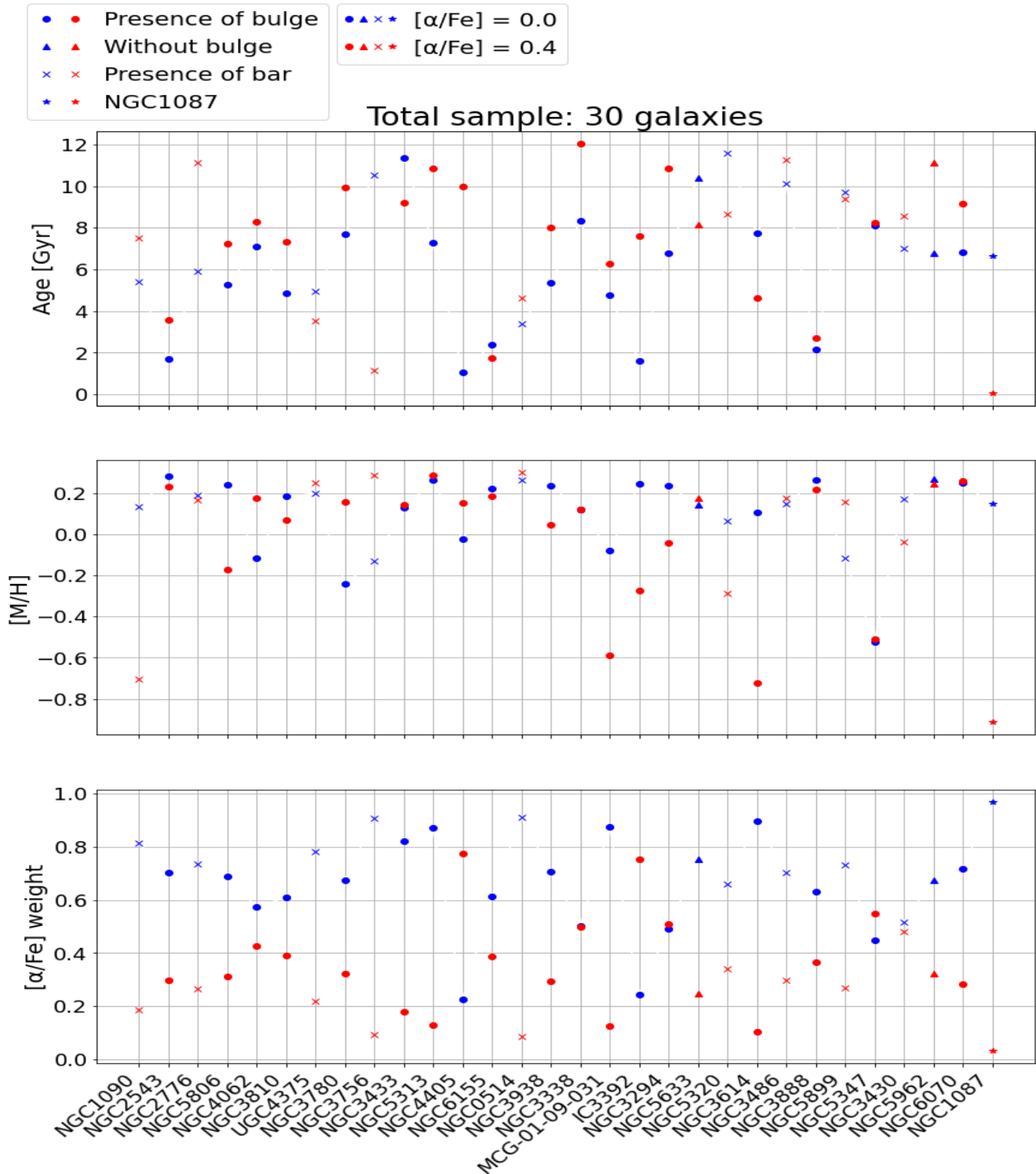
Fig. 12. Mean mass-weighted age (top panel), [M/H] (middle panel) and $[\alpha/\mathrm{Fe}]$ weights (bottom panel) obtained for each one of the galaxies of the sample. Galaxies with bulge (dot), without bulge (triangle), with bar (cross) and NGC1087 (star) are distinguished.

a) All the galaxies from the sample

b) Barred galaxies from the sample
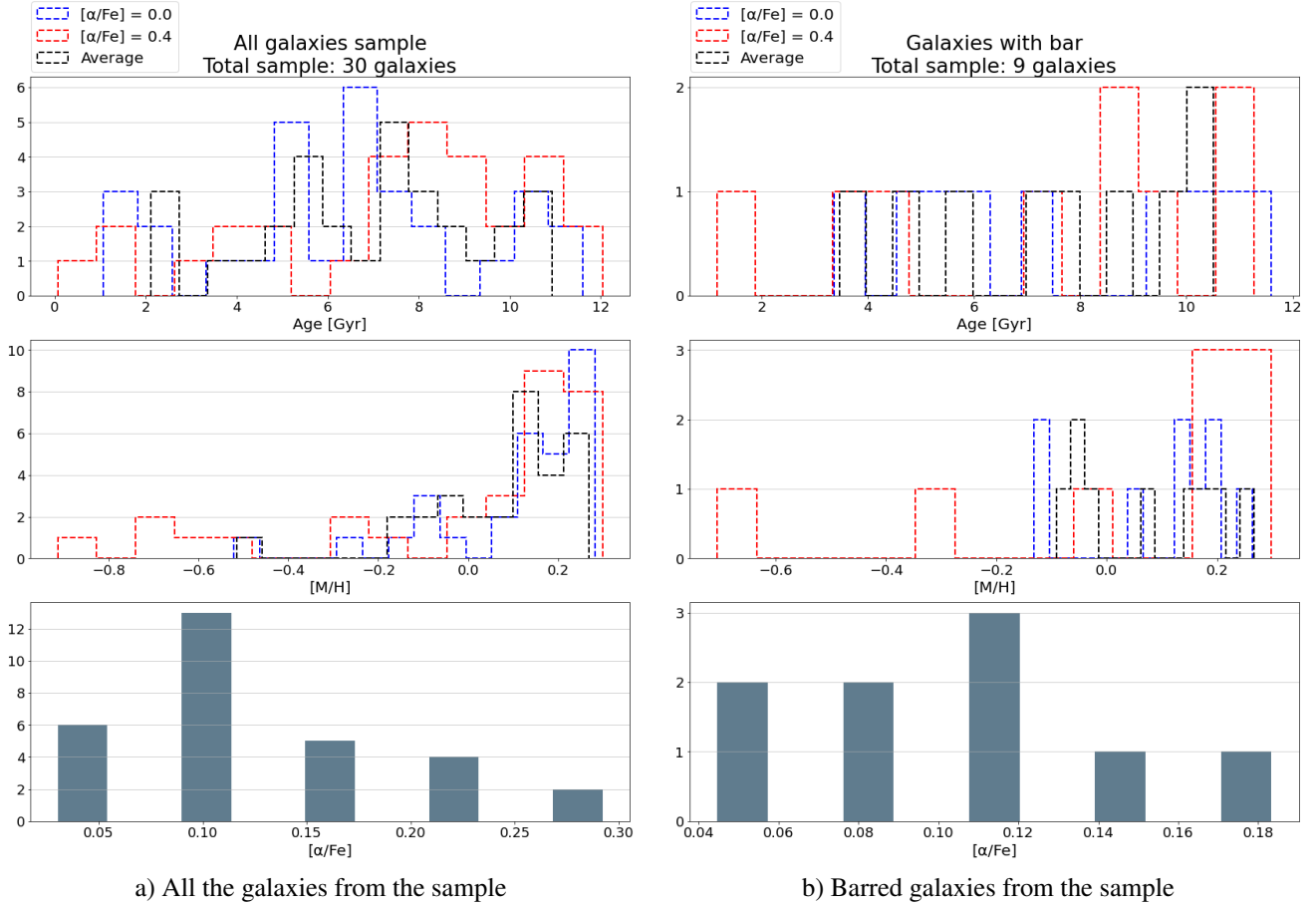
Fig. 13. Mean mass-weighted age (top panel), [M/H] (middle panel) and $[\alpha/\mathrm{Fe}]$ weights (bottom panel) histograms for both the whole galaxy sample bulges or centers (left) and the barred galaxy subsample bulges (right). In the two top panels, the $[\alpha/\mathrm{Fe}] = 0$ (blue), $[\alpha/\mathrm{Fe}] = 4$ (red) and average results are shown.

From Figure 13, it is clear that the average age distribution covers almost all the range from the templates. Some peaks are noticed around young (~ 2.5 Gyr), intermediate (~ 5.5 and ~ 7.5 Gyr) and old (~ 11 Gyr) ages. It is worth noticing that $[\alpha/\mathrm{Fe}] = 0$ ages show two remarkable peaks (at ages ~ 5 and 7 Gyr, while the $[\alpha/\mathrm{Fe}] = 0.4$ ones show also two peaks, but at higher ages (~ 8 and 11 Gyr) and in a wider distribution in the histogram. For the barred subsample, the age histogram seems more homogeneous, with higher incidence at the highest values (~ 10.5 Gyr) for both $[\alpha/\mathrm{Fe}]$. Most of the results for both $[\alpha/\mathrm{Fe}]$ tend to metal-rich values (in solar terms) for the entire sample. For the barred subsample, the results are more distributed between $[\mathrm{M/H}] \sim -0.1$ and 0.3, with a tendency for high metallicities. The values found at $[\mathrm{M/H}] \sim 0.3$ may be biased by the metallicity upper range ending close to that value, while the lowest values do not go beyond $[\mathrm{M/H}] = -0.7$ even when there are more metal-poor templates. Finally, the $[\alpha/\mathrm{Fe}]$ histogram shows that the most common value is ~ 0.1, indicating a dominating slow-paced star formation for the majority of galaxies in the sample. The barred subsample shows a more equal distribution of both $[\alpha/\mathrm{Fe}]$ templates' weights, but still inclined to the lowest values of the sample.

In order to look for possible correlations between the bulge mass and both its age and metallicity composition, Figure 14 has been elaborated. There seems to be no correlation between the bulge mass and its age or metallicity from this figure, but it is remembered that there is a bias in the bulge mass due to the BEARD sample selection. However, the star formation timescale appears to change with the bulge mass for this range. For lower masses of the bulge ($\sim 10^{7.5}$ $M_\odot$), fast or slow-paced star formation may occur, depending on the galaxy, and no tendency is clear, although this could be due to small number statistics for that bulge mass values. For higher mass values ($\gtrsim 10^{8.2}$ $M_\odot$), the $[\alpha/\mathrm{Fe}] = 0$ stellar populations seem to dominate over the 0.4 ones. This would mean that more massive bulges in disk galaxies tend to slowdown the stellar formation, while less massive ones may have either fast or slow formation processes. This is contrary to what happens in ellipticals, see Fig. 4 from (Thomas and Davies, 2006). The presence of a bar does not seem to affect such possible behaviour.

Since the bulge mass range covered by the sample is biased, it is difficult to conclude if there are relations between the bulge parameters and its mass. As a way of corroborating the results with our method, some data from CALIFA have been retrieved to compare with (Figure 15). The used values have been obtained from C2D (Méndez-Abreu et al., 2019), which generates a datacube prepared for spectrophotometric decompositions from the initial datacubes of CALIFA DR3 (Sánchez et al., 2016). The age values seem to disperse at low bulge masses ($\lesssim 10^{10}$ $M_\odot$) in the CALIFA sample. Such dispersion and the trend of the values are coherent with our results. Regarding the metallicity, the values obtained from our methodology appear to be higher than those from CALIFA for the same masses. This is most likely due to the different stellar libraries used in the CALIFA's pipeline, Pipe3D (Sánchez et al., 2016), and our work. Pipe3D makes use of the GSD156 library of SSPs, covering 39 ages from 1 Myr to 14.1 Gyr and 4 metallicities from [M/H]=-0.70 to 0.18. Hence, the results shown from CALIFA data are enclosed to [M/H] values lower than the ones used in our study.

Another comparison of our results with other works has been made by representing the $[\alpha/\mathrm{Fe}]$ vs σ curve (Figure 16). From Morelli et al. (2008) and Morelli et al. (2016), where isolated and cluster galaxies where studied, respectively, it was found that there is a possible correlation between the velocity dispersion and the $[\alpha/\mathrm{Fe}]$ for different bulges of disk galaxies. Our sample mainly contains isolated galaxies or galaxies located in low-density environments. Most of them lead to results that locate inside the trend from Morelli's works, except for two outliers, that are IC3392 and NGC4405. No different trends have been found for the bulgeless or barred subsamples.
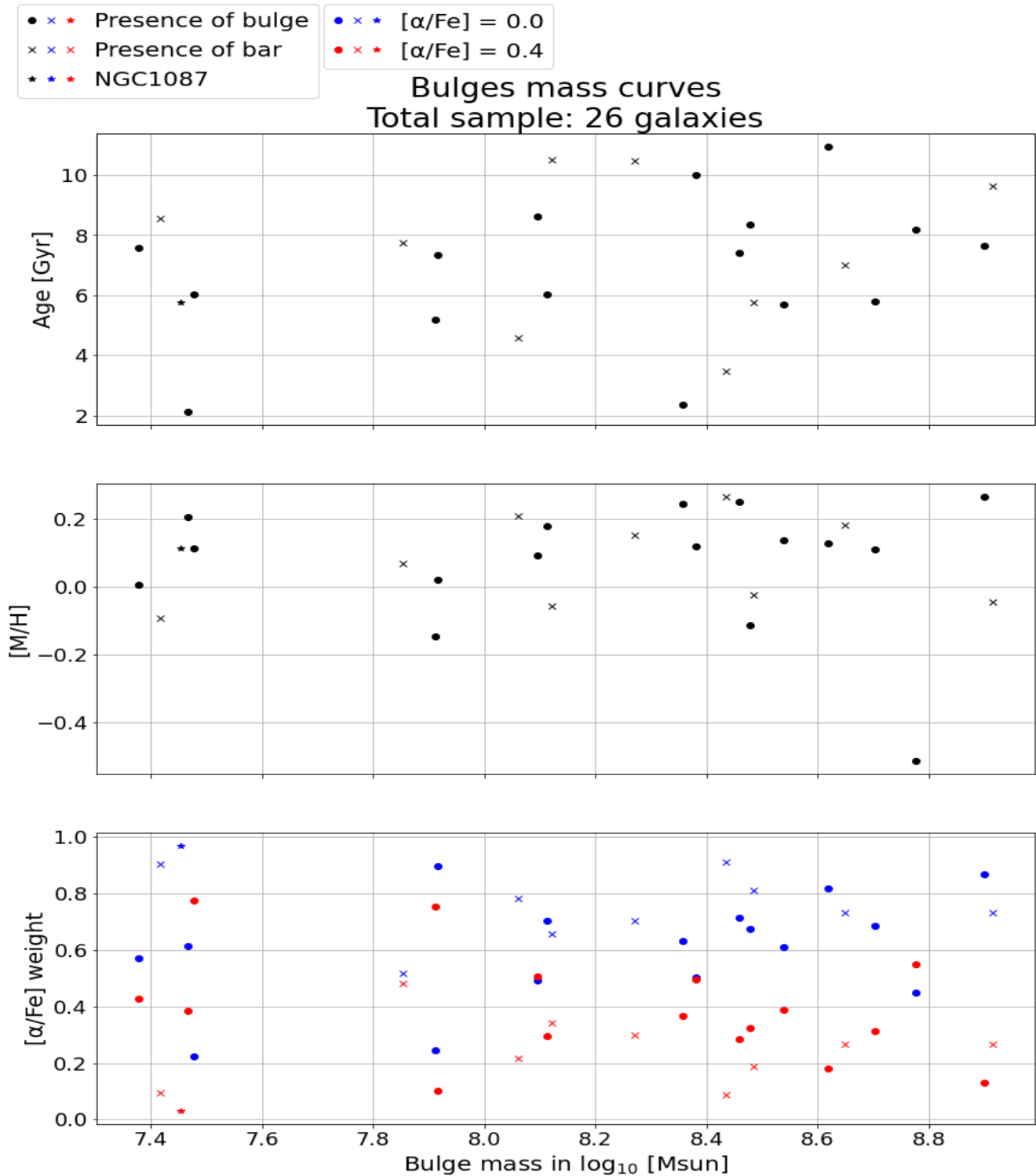
Fig. 14. Mean mass-weighted age (top panel), [M/H] (intermediate panel) and $[\alpha/\mathrm{Fe}]$ (bottom panel) weights vs bulge mass. Galaxies with bulge (dot), without bulge (triangle), with bar (cross) and NGC1087 (star) are distinguished. For the two top panels, the average values are shown, while for the bottom one both $[\alpha/\mathrm{Fe}] = 0$ (blue) and 0.4 (red) are given.
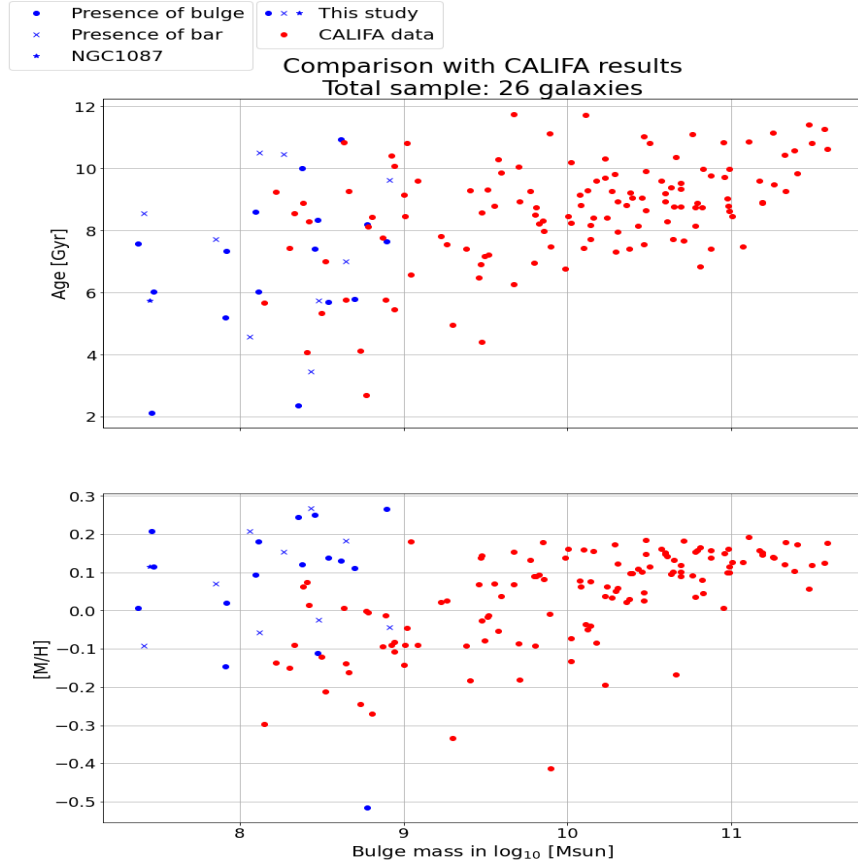
Fig. 15. Mean mass-weighted age (top panel) and metallicity (bottom panel) vs bulge mass. Comparison between our results (blue) and CALIFA's (red). Galaxies from our sample with bulge (blue dot), with bar (blue cross) and NGC1087 (blue star) are distinguished.
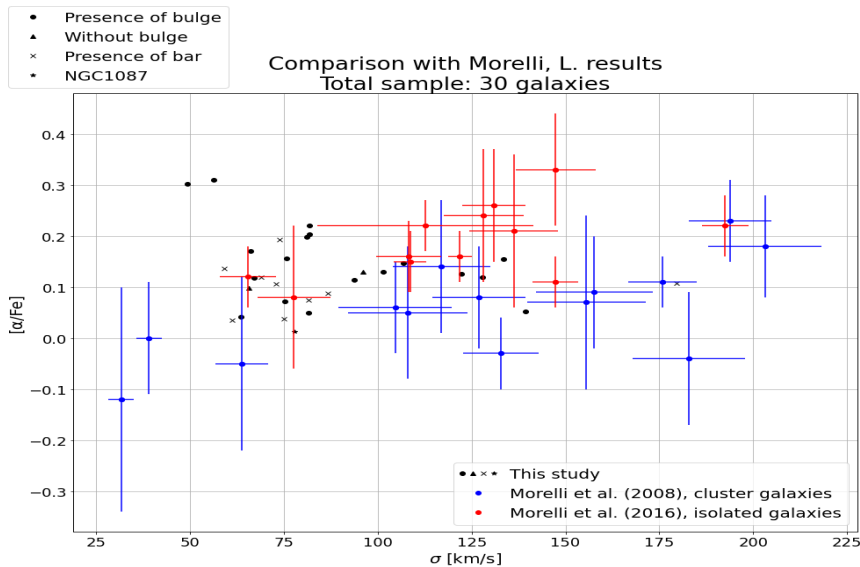
Fig. 16. Curve showing the relation between $[\alpha/\mathrm{Fe}]$ and σ, both for our results and for the ones obtained by Morelli et al. (2008) and Morelli et al. (2016). Galaxies from our sample with bulge (black dot), without bulge (black triangle), with bar (black cross) and NGC1087 (black star) are distinguished.

6. Conclusions

The stellar kinematic and populations analyses have been performed for the galaxies in the BEARD sample, retrieving such results both for their bulges and radial profiles. The S/N=30 threshold selected for the different spectra to analyse has allowed to study results that are reliable for the goals we have established. In order to have a picture of the possible trends followed by similar galaxies, the analysis has been focused into the results from the bulges' (or centers, for pure bulgeless galaxies) spectra altogether, leaving the detailed analysis of the radial profiles as future work.

In the entire sample, there are 9 barred galaxies. For these galaxies, the central/bulge LOSVD velocity dispersion stays below ~ 90 km/s, while different galaxies with bulge cover both low and high dispersion values, some of them trespassing such value. This is in agreement with the barred galaxies being bulgeless and may hint to them having disk-like bulges, which have lower dispersion than classical ones. One exception on this behaviour for barred galaxies is NGC5899, which is the one with the most massive bulge from the complete sample. This exception has lead to search for a possible relation between the bulge mass and its velocity dispersion, finding that more massive bulges tend to higher velocity dispersion values. However, the BEARD sample selection of massive disk galaxies with low mass bulges complicates coming to strong correlations involving the bulge mass.

From the populations analysis, it has not been observed that different types of galaxies present significant changes in the age or metallicity distribution. What has been found is that all the bulges/centres from the sample include a dominating $[\alpha/\text{Fe}] = 0$ stellar population. This implies extended non-monolithic stellar formation, contrary to what is expected from classical bulges. Also, all galaxies with bulge and without a bar, except for three, have shown older ages for the fast-forming ($[\alpha/\text{Fe}] = 0.4$) stellar population of the bulge than for the slow-paced one, which can be understood as an old population formed in a short burst long ago, followed by a younger formation process more extended in time. While the ages distribution does not form clear groups, the two most common values have been found around ~ 5.5 and ~ 7.5 Gyr. For the metallicity, it has been concluded that the sample tends to metal-rich values in solar terms. $[\alpha/\text{Fe}] = 0.4$ stellar populations usually reach lower metallicity values than the $[\alpha/\text{Fe}] = 0$ ones. Generally, the results incline to a low $[\alpha/\text{Fe}]$, indicating that slow-paced star formation dominates the galaxies from the studied sample.

A correlation between the bulge mass and the stellar populations properties has been searched. While this has not been found for age and metallicity values, there seems to be an association between the stellar formation timescale and the bulge's mass. For the lowest bulge masses ($\sim 10^{7.5}$ M$_\odot$), fast or slow-paced star formation may occur, but for higher values ($\gtrsim 10^{8.2}$ M$_\odot$), the $[\alpha/\text{Fe}] = 0$ stellar populations seem to dominate over the 0.4 ones. This would mean that more massive bulges tend to a slowdown of stellar formation, which is contrary to what happens in ellipticals (Thomas and Davies, 2006). Nevertheless, it is remembered that this result may be biased by the BEARD sample selection.

To try to test the reliability of our results, they have been compared to CALIFA DR3 (Sánchez et al., 2016) bulges values of age and metallicity versus the bulge mass. There seems to be an agreement for the ages tendency with our data, but a difference is found when comparing the metallicity values, where our results lay at slightly metal-richer values than CALIFA's for the same bulge masses. This could be due to CALIFA's pipeline used library (GSD156) being limited to an upper bound of $[M/H] = 0.18$, lower than the one from our used templates, which is $[\text{M}/\text{H}] = 0.4$. Another comparison has been done

by seeing the correlation between $[\alpha/\text{Fe}]$ and σ in perspective with the results obtained by Morelli et al. (2008, 2016) for cluster and isolated galaxies, respectively. Except for two outliers, our results lay inside the error of such previous studies. Therefore, both the CALIFA DR3 data and the results obtained by Morelli, L., are in agreement with ours.

Despite having marked different types of galaxies in our sample (with bulge, bulgeless, barred and the complex galaxy NGC1087), no different trends have been found for them, apart from the seemingly lower values of the LOSVD velocity dispersion for barred galaxies. There is also the fact that barred galaxies with bulge and pure bulgeless galaxies do not necessary follow the possible trends of galaxies with simply a bulge. However, this may be due to the low subsample of these type of galaxies, specially the bulgeless ones. The barred trends analysis could be improved by increasing the total sample of galaxies to the whole BEARD sample, while almost all of the pure bulgeless galaxies from the BEARD sample are already included in this work. The in-depth analysis of the radial profiles might shed some light at these aspects. Such study is left as future work, since the methical study of the behaviour of each radial profile goes beyond the available time for the elaboration of this current work.

References

Aguerri, J. A. L., Elias-Rosa, N., Corsini, E. M., and Muñoz-Tuñón, C. (2005). Photometric properties and origin of bulges in SB0 galaxies. *A&A*, 434(1):109–122.

Avila-Reese, V., Zavala, J., and Lacerna, I. (2014). The growth of galactic bulges through mergers in Λ cold dark matter haloes revisited - II. Morphological mix evolution. *MNRAS*, 441(1):417–430.

Barazza, F. D., Jogee, S., and Marinova, I. (2008). Bars in Disk-dominated and Bulge-dominated Galaxies at z ∼0: New Insights from ∼3600 SDSS Galaxies. *ApJ*, 675(2):1194–1212.

Bender, R., Burstein, D., and Faber, S. M. (1992). Dynamically Hot Galaxies. I. Structural Properties. *ApJ*, 399:462.

Böker, T., Laine, S., van der Marel, R. P., Sarzi, M., Rix, H.-W., Ho, L. C., and Shields, J. C. (2002). A Hubble Space Telescope Census of Nuclear Star Clusters in Late-Type Spiral Galaxies. I. Observations and Image Analysis. *AJ*, 123(3):1389–1410.

Bournaud, F., Elmegreen, B. G., and Elmegreen, D. M. (2007). Rapid Formation of Exponential Disks and Bulges at High Redshift from the Dynamical Evolution of Clump-Cluster and Chain Galaxies. *ApJ*, 670(1):237–248.

Brooks, A. and Christensen, C. (2016). Bulge Formation via Mergers in Cosmological Simulations. In Laurikainen, E., Peletier, R., and Gadotti, D., editors, *Galactic Bulges*, volume 418 of *Astrophysics and Space Science Library*, page 317.

Cappellari, M. (2002). Efficient multi-Gaussian expansion of galaxies. *MNRAS*, 333(2):400–410.

Cenarro, A. J., Cardiel, N., Gorgas, J., Peletier, R. F., Vazdekis, A., and Prada, F. (2001). Empirical calibration of the near-infrared Ca ii triplet - I. The stellar library and index definition. *MNRAS*, 326(3):959–980.

Ceverino, D., Dekel, A., Tweed, D., and Primack, J. (2015). Early formation of massive, compact, spheroidal galaxies with classical profiles by violent disc instability or mergers. *MNRAS*, 447(4):3291–3310.

Costantin, L., Méndez-Abreu, J., Corsini, E. M., Morelli, L., Aguerri, J. A. L., Dalla Bontà, E., and Pizzella, A. (2017). No evidence for small disk-like bulges in a sample of late-type spirals. *A&A*, 601:A84.

Eggen, O. J., Lynden-Bell, D., and Sandage, A. R. (1962). Evidence from the motions of old stars that the Galaxy collapsed. *ApJ*, 136:748.

Faber, S. M. and Jackson, R. E. (1976). Velocity dispersions and mass-to-light ratios for elliptical galaxies. *ApJ*, 204:668–683.

Falcón-Barroso, J., Peletier, R. F., and Balcells, M. (2002). Bulges on the Fundamental Plane of early-type galaxies. *MNRAS*, 335(3):741–752.

Falcón-Barroso, J., Sánchez-Blázquez, P., Vazdekis, A., Ricciardelli, E., Cardiel, N., Cenarro, A. J., Gorgas, J., and Peletier, R. F. (2011). An updated MILES stellar library and stellar population models. *A&A*, 532:A95.

Fisher, D. B. and Drory, N. (2016). An Observational Guide to Identifying Pseudobulges and Classical Bulges in Disc Galaxies. In Laurikainen, E., Peletier, R., and Gadotti, D., editors, *Galactic Bulges*, volume 418 of *Astrophysics and Space Science Library*, page 41.

Graham, A. W. and Driver, S. P. (2005). A Concise Reference to (Projected) Sérsic $R^{1/n}$ Quantities, Including Concentration, Profile Slopes, Petrosian Indices, and Kron Magnitudes. *PASA*, 22(2):118–127.

Grand, R. J. J., Gómez, F. A., Marinacci, F., Pakmor, R., Springel, V., Campbell, D. J. R., Frenk, C. S., Jenkins, A., and White, S. D. M. (2017). The Auriga Project: the properties and formation mechanisms of disc galaxies across cosmic time. *MNRAS*, 467(1):179–207.

Hopkins, P. F., Cox, T. J., Younger, J. D., and Hernquist, L. (2009). How do Disks Survive Mergers? *ApJ*, 691(2):1168–1201.

Hubble, E. P. (1925). Cepheids in spiral nebulae. *The Observatory*, 48:139–142.

Hubble, E. P. (1926). Extragalactic nebulae. *ApJ*, 64:321–369.

Immeli, A., Samland, M., Gerhard, O., and Westera, P. (2004). Gas physics, disk fragmentation, and bulge formation in young galaxies. *A&A*, 413:547–561.

Karachentsev, I. (1989). Thin Edge-On Galaxies as a Tool for the Investigation of Large-Scale Streaming Motions in the Universe. *AJ*, 97:1566.

Karachentsev, I. D., Karachentseva, V. E., Kudrya, Y. N., Sharina, M. E., and Parnovskij, S. L. (1999). The revised Flat Galaxy Catalogue. *Bulletin of the Special Astrophysics Observatory*, 47:5–185.

Karachentsev, I. D., Karachentseva, V. E., and Parnovskij, S. L. (1993). Flat galaxies catalogue. *Astronomische Nachrichten*, 314(3):97–222.

Kauffmann, G. (1996). The age of elliptical galaxies and bulges in a merger model. *MNRAS*, 281(2):487–492.

Kautsch, S. J. (2009). The Edge-On Perspective of Bulgeless, Simple Disk Galaxies. *PASP*, 121(886):1297.

Kormendy, J. and Bender, R. (1996). A Proposed Revision of the Hubble Sequence for Elliptical Galaxies. *ApJ*, 464:L119.

Kormendy, J., Drory, N., Bender, R., and Cornell, M. E. (2010). Bulgeless Giant Galaxies Challenge Our Picture of Galaxy Formation by Hierarchical Clustering. *ApJ*, 723(1):54–80.

Larson, R. B. (1974). Dynamical models for the formation and evolution of spherical galaxies. *MNRAS*, 166:585–616.

Méndez-Abreu, J., Ruiz-Lara, T., Sánchez-Menguiano, L., de Lorenzo-Cáceres, A., Costantin, L., Catalán-Torrecilla, C., Florido, E., Aguerri, J. A. L., Bland-Hawthorn, J., Corsini, E. M., Dettmar, R. J., Galbany, L., García-Benito, R., Marino, R. A., Márquez, I., Ortega-Minakata, R. A., Papaderos, P., Sánchez, S. F., Sánchez-Blazquez, P., Spekkens, K., van de Ven, G., Wild, V., and Ziegler, B. (2017). Two-dimensional multi-component photometric decomposition of CALIFA galaxies. *A&A*, 598:A32.

Méndez-Abreu, J., Sánchez, S. F., and de Lorenzo-Cáceres, A. (2019). Star formation in CALIFA early-type galaxies: a matter of discs. *MNRAS*, 488(1):L80–L84.

Mitronova, S. N., Karachentsev, I. D., Karachentseva, V. E., Jarrett, T. H., and Kudrya, Y. N. (2004). The 2MASS-selected Flat Galaxy Catalog. *Bulletin of the Special Astrophysics Observatory*, 57:5–163.

Morelli, L., Parmiggiani, M., Corsini, E. M., Costantin, L., Dalla Bontà, E., Méndez-Abreu, J., and Pizzella, A. (2016). Stellar populations in the bulges of isolated galaxies. *MNRAS*, 463(4):4396–4421.

Morelli, L., Pompei, E., Pizzella, A., Méndez-Abreu, J., Corsini, E. M., Coccato, L., Saglia, R. P., Sarzi, M., and Bertola, F. (2008). Stellar populations of bulges in 14 cluster disc galaxies. *MNRAS*, 389(1):341–363.

Noguchi, M. (1999). Early Evolution of Disk Galaxies: Formation of Bulges in Clumpy Young Galactic Disks. *ApJ*, 514(1):77–95.

Pietrinferni, A., Cassisi, S., Salaris, M., and Castelli, F. (2004). A Large Stellar Evolution Database for Population Synthesis Studies. I. Scaled Solar Models and Isochrones. *ApJ*, 612(1):168–190.

Pietrinferni, A., Cassisi, S., Salaris, M., and Castelli, F. (2006). A Large Stellar Evolution Database for Population Synthesis Studies. II. Stellar Models and Isochrones for an α-enhanced Metal Distribution. *ApJ*, 642(2):797–812.

Pipino, A., D'Ercole, A., and Matteucci, F. (2008). Formation of [α/Fe] radial gradients in the stars of elliptical galaxies. *A&A*, 484(3):679–691.

Sánchez, S. F., Pérez, E., Sánchez-Blázquez, P., García-Benito, R., Ibarra-Mede, H. J., González, J. J., Rosales-Ortega, F. F., Sánchez-Menguiano, L., Ascasibar, Y., Bitsakis, T., Law, D., Cano-Díaz, M., López-Cobá, C., Marino, R. A., Gil de Paz, A., López-Sánchez, A. R., Barrera-Ballesteros, J., Galbany, L., Mast, D., Abril-Melgarejo, V., and Roman-Lopes, A. (2016). Pipe3D, a pipeline to analyze Integral Field Spectroscopy Data: II. Analysis sequence and CALIFA dataproducts. *Rev. Mexicana Astron. Astrofis.*, 52:171–220.

Sánchez-Blázquez, P. (2016). Stellar Populations of Bulges at Low Redshift. In Laurikainen, E., Peletier, R., and Gadotti, D., editors, *Galactic Bulges*, volume 418 of *Astrophysics and Space Science Library*, page 127.

Sánchez-Blázquez, P., Ocvirk, P., Gibson, B. K., Pérez, I., and Peletier, R. F. (2011). Star formation history of barred disc galaxies. *MNRAS*, 415(1):709–731.

Sánchez-Blázquez, P., Peletier, R. F., Jiménez-Vicente, J., Cardiel, N., Cenarro, A. J., Falcón-Barroso, J., Gorgas, J., Selam, S., and Vazdekis, A. (2006). Medium-resolution Isaac Newton Telescope library of empirical spectra. *MNRAS*, 371(2):703–718.

Scannapieco, C., White, S. D. M., Springel, V., and Tissera, P. B. (2009). The formation and survival of discs in a ΛCDM universe. *MNRAS*, 396(2):696–708.

Schaye, J., Crain, R. A., Bower, R. G., Furlong, M., Schaller, M., Theuns, T., Dalla Vecchia, C., Frenk, C. S., McCarthy, I. G., Helly, J. C., Jenkins, A., Rosas-Guevara, Y. M., White, S. D. M., Baes, M., Booth, C. M., Camps, P., Navarro, J. F., Qu, Y., Rahmati, A., Sawala, T., Thomas, P. A., and Trayford, J. (2015). The EAGLE project: simulating the evolution and assembly of galaxies and their environments. *MNRAS*, 446(1):521–554.

Scholz-Díaz, L., Martín-Navarro, I., and Falcón-Barroso, J. (2022). The dark side of galaxy stellar populations - I. The stellar-to-halo mass relation and the velocity dispersion-halo mass relation. *MNRAS*, 511(4):4900–4920.

Shapley, H. and Curtis, H. D. (1921). The Scale of the Universe. *Bulletin of the National Research Council*, 2(11):171–217.

Tacchella, S., Dekel, A., Carollo, C. M., Ceverino, D., DeGraf, C., Lapiner, S., Mandelker, N., and Primack, J. R. (2016). Evolution of density profiles in high-z galaxies: compaction and quenching inside-out. *MNRAS*, 458(1):242–263.

Thomas, D. and Davies, R. L. (2006). Rejuvenation of spiral bulges. *MNRAS*, 366(2):510–520.

Vazdekis, A., Cenarro, A. J., Gorgas, J., Cardiel, N., and Peletier, R. F. (2003). Empirical calibration of the near-infrared CaII triplet - IV. The stellar population synthesis models. *MNRAS*, 340(4):1317–1345.

Vazdekis, A., Coelho, P., Cassisi, S., Ricciardelli, E., Falcón-Barroso, J., Sánchez-Blázquez, P., La Barbera, F., Beasley, M. A., and Pietrinferni, A. (2015). Evolutionary stellar population synthesis with MILES - II. Scaled-solar and α-enhanced models. *MNRAS*, 449(2):1177–1214.

Zavala, J., Avila-Reese, V., Firmani, C., and Boylan-Kolchin, M. (2012). The growth of galactic bulges through mergers in Λ CDM haloes revisited - I. Present-day properties. *MNRAS*, 427(2):1503–1516.

Zibetti, S., Charlot, S., and Rix, H.-W. (2009). Resolved stellar mass maps of galaxies - I. Method and implications for global mass estimates. *MNRAS*, 400(3):1181–1198.

Zolotov, A., Dekel, A., Mandelker, N., Tweed, D., Inoue, S., DeGraf, C., Ceverino, D., Primack, J. R., Barro, G., and Faber, S. M. (2015). Compaction and quenching of high-z galaxies in cosmological simulations: blue and red nuggets. *MNRAS*, 450(3):2327–2353.

Zwicky, F. (1933). Die Rotverschiebung von extragalaktischen Nebeln. *Helvetica Physica Acta*, 6:110–127.

Galaxy	Galaxy mass [$M_\odot$]	Maximum radius [arcsec]	r_{bd} [arcsec]	Bulge mass [$M_\odot$]	Bulge S/N	Bulge $<\log\text{Age}>_{0.0}$ [Gyr]	Bulge $<\log\text{Age}>_{0.4}$ [Gyr]	Bulge $<[M/H]>_{0.0}$	Bulge $<[M/H]>_{0.4}$
IC3392	$10^{10.08}$	125.12	1.98	$10^{7.92}$	93.44	0.20	0.88	0.25	−0.27
MCG-01-09-031	$10^{10.14}$	4.28	3.17	-	136.18	0.68	0.80	−0.08	−0.59
NGC0514	$10^{10.19}$	1.29	2.38	$10^{8.43}$	55.24	0.53	0.66	0.26	0.30
NGC1087	$10^{10.08}$	35.12	1.98	$10^{7.45}$	70.62	0.82	−1.19	0.15	−0.91
NGC1090	$10^{10.63}$	16.92	4.36	$10^{8.48}$	92.02	0.73	0.88	0.13	−0.71
NGC2543	$10^{10.59}$	1.69	5.15	-	44.57	0.23	0.55	0.28	0.23
NGC2701	$10^{10.24}$	1.69	-	-	17.34	0.81	−0.96	0.14	0.14
NGC2742	$10^{10.08}$	-	2.38	$10^{7.50}$	18.85	0.79	0.74	0.18	0.15
NGC2776	$10^{10.55}$	17.81	3.96	$10^{8.65}$	108.29	0.77	1.05	0.19	0.16
NGC3294	$10^{10.37}$	30.55	2.38	$10^{8.10}$	88.09	0.83	1.04	0.24	−0.04
NGC3338	$10^{10.02}$	5.42	4.36	$10^{8.38}$	97.08	0.92	1.08	0.12	0.12
NGC3430	$10^{10.09}$	3.02	2.77	$10^{7.85}$	44.49	0.85	0.93	0.17	−0.04
NGC3433	$10^{10.43}$	2.79	5.15	$10^{8.62}$	70.50	1.05	0.96	0.13	0.14
NGC3486	$10^{10.17}$	19.03	4.75	$10^{8.27}$	163.67	1.01	1.05	0.15	0.17
NGC3614	$10^{10.10}$	3.40	2.77	$10^{7.92}$	62.87	0.89	0.67	0.11	−0.72
NGC3756	$10^{10.04}$	-	1.98	$10^{7.42}$	36.98	1.02	0.07	−0.13	0.29
NGC3780	$10^{10.49}$	3.28	3.17	$10^{8.48}$	48.93	0.88	1.00	−0.24	0.16
NGC3810	$10^{10.20}$	24.70	4.75	$10^{8.54}$	186.27	0.69	0.87	0.18	0.07
NGC3888	$10^{10.32}$	8.76	2.38	$10^{8.36}$	49.11	0.33	0.43	0.26	0.21
NGC3938	$10^{10.11}$	23.08	4.75	$10^{8.11}$	141.77	0.73	0.90	0.24	0.05
NGC4062	$10^{10.25}$	11.74	1.98	$10^{7.38}$	48.73	0.85	0.92	−0.12	0.18
NGC4405	$10^{10.05}$	94.12	1.19	$10^{7.48}$	92.83	0.03	1.00	−0.02	0.15
NGC5313	$10^{10.97}$	20.92	4.36	$10^{8.90}$	137.57	0.86	1.04	0.26	0.29
NGC5320	$10^{10.33}$	160.65	1.98	$10^{8.12}$	50.43	1.06	0.94	0.06	−0.29
NGC5347	$10^{10.30}$	4.03	6.34	$10^{8.78}$	73.39	0.91	0.92	−0.52	−0.51
NGC5633	$10^{10.22}$	17.01	-	-	43.69	1.02	0.91	0.14	0.18
NGC5806	$10^{10.41}$	135.20	7.92	$10^{8.70}$	175.50	0.72	0.86	0.24	−0.17
NGC5899	$10^{10.23}$	87.82	4.36	$10^{8.91}$	123.83	0.99	0.97	−0.12	0.16
NGC5962	$10^{10.06}$	18.9	-	-	111.67	0.83	1.05	0.27	0.25
NGC6070	$10^{10.06}$	5.29	4.36	$10^{8.46}$	71.98	0.83	0.96	0.25	0.26
NGC6155	$10^{10.10}$	61.11	1.58	$10^{7.47}$	72.08	0.38	0.24	0.22	0.19
UGC4375	$10^{10.07}$	1.59	1.98	$10^{8.06}$	37.06	0.69	0.55	0.20	0.25
UGC4621	$10^{10.18}$	-	-	-	6.56	0.76	1.01	−0.32	0.12

Table 3: The first column contains the names of the galaxies from the analysed sample. The second column shows the galaxy mass in solar masses. The third column contains the maximum extension for each galaxy imposing a minimal S/N= 30 for the bin. The following columns are, respectively, the bulge-disk radius from the photometric decomposition, the bulge mass in solar masses, the S/N from the integrated bulge, the logarithm of the mean age for the templates with [α/Fe] = 0 and 0.4, and the mean metallicity for the templates with [α/Fe] = 0 and 0.4.